LA-UR- 95-3516

CONF-9510253--1

Los Alamos National Laboratory is operated by the University of California for the United States Department of Energy under contract W-7405-ENG-36



TITLE: SATURATION OF RADIATION-INDUCED PARAMETRIC INSTABILITIES BY EXCITATION OF LANGMUIR TURBULENCE

AUTHOR(S): D.F. Dubois, T-13
H.A. Rose, T-13
D. Russell, Lodestar Research Inc

SUBMITTED TO: INTERNATIONAL TOPICAL PLASMA PHYSICS WORKSHOP, 16-20 OCTOBER, 1995, TRIESTE, ITALY



Los Alamos

Los Alamos National Laboratory
Los Alamos, New Mexico 87545

FORM NO. 836 R4
ST. NO. 2629 5/81

# SATURATION OF RADIATION-INDUCED PARAMETRIC INSTABILITIES BY EXCITATION OF LANGMUIR TURBULENCE*

D.F.DUBOIS[1], Harvey A. Rose[1], and David Russell[2]

[1]Complex Systems Group, MS B213
Theoretical Division
Los Alamos National Laboratory
Los Alamos , New Mexico, 87545

[2]Lodestar Research Inc.
2400 Central Ave.
Boulder CO.,80301

ABSTRACT

Progress made in the last few years in the calculation of the saturation spectra of parametric instabilities which involve Langmuir daughter waves will be reviewed. These instabilities include the ion acoustic decay instability , the two plasmon decay instability (TPDI), and stimulated Raman scattering (SRS). In particular I will emphasize spectral signatures which can be directly compared with experiment. The calculations are based on reduced models of driven Langmuir turbulence.Thomson scattering from hf-induced Langmuir turbulence in the unpreconditioned ionosphere has resulted in detailed agreement between theory and experiment at early times. Strong turbulence signatures dominate in this regime where the weak turbulence approximation fails completely. Recent experimental studies of the TPDI have measured the Fourier spectra of Langmuir waves as well as the angular and frequency spectra of light emitted near 3/2 of the pump frequency again permitting some detailed comparisons with theory. The experiments on SRS are less detailed but by Thomson scattering the secondary decay of the daughter Langmuir wave has been observed. Scaling laws derived from a local model of SRS saturation are compared with full simulations and recent Nova experiments.

*Based on a paper to be presented at the International Topical Plasma Physics Workshop/Symposium: Coherent Processes in Nonlinear Media, 16-20 October, 1995 at the International Center for Theoretical Physics, Trieste, Italy. Research supported by the US Department of Energy.

## 1.Introduction

Parametric instablities excited in plasmas by coherent electromagnetic radiation continue to be subjects of intense experimental interest for both the laser induced inertial confinement fusion (ICF) and RF modification of the ionosphere. Megajoule, Nd glass lasers, frequency tripled to a wavelength of $0.351\,\mu m$ , with pulse lengths of tens of ns, designed to drive cm scale targets, are planned both in France and in the US: the National Ignition Facility (NIF). A large ionospheric modification facility, the Highpower Active Auroral Research Project (HAARP) is being constructed in Alaska and the heating facility at Arecibo, Puerto Rico is being upgraded. These parametric instabilities, which have been studied for over 30 years, are expected to play a central role in the interaction of these high power electromagnetic sources with the relevant plasmas. While the linear theory of these instabilities has been treated in considerable detail the theory of their nonlinear saturation is still developing. The experimental diagnostics and numerical modeling techniques have improved to the level that detailed comparison between theory and observations can now be made. It is important to have reliable models which can treat realistic problems for these applications. The goal of our recent research has been to compare the predictions of these models with well diagnosed experiments to establish the validity of the modeling.

In this paper I will review recent work on the nonlinear saturation of three parametric instabilities: the ion acoustic decay (IAD)instability [1 ], the two plasmon decay (TPD) instability [2], and stimulated Raman scattering (SRS) [3,4]. These instabilities excite high levels of Langmuir waves (LWs) in a narrow domain in k space and saturate in a state of Langmuir turbulence in which the wave energy is spread out in k space primarily by wave-wave interactions.

Recent experiments have been carried out by workers from Lawrence Livermore and Los Alamos National Laboratories using targets on the NOVA laser which emulate certain plasma conditions expected for indirect drive targets proposed for the NIF. Signatures of SRS, SBS (stimulated Brillouin scattering), TPD and filamantation have been observed for these targets usually at programatically acceptable levels For direct drive targets considered for the NIF the density scale lengths near critical and quarter critical density are larger and IADI and TPD may be stronger. The nonlinear evolution of IAD instability and its related modulational instability has been the subject of several beautifully detailed observations using the RF heating and incoherent scatter radar facilities at Arecibo,

Puerto Rico which have produced detailed verification of predictions of Langmuir collapse phenomena.

I will focus on nonlinear physics which appears to be generic for these instabilities and on theoretical predictions which have been compared with experiment. Reduced descriptions , which are hydrodynamical-like models, which can be derived as approximations to Vlasov theory [5], have been the principal tools for obtaining these predictions. These models provide nonlinear partial differential equations for the evolution of the complex envelope, $\mathbf{E}(\mathbf{x},t)$, of the Langmuir electric field which we write as $1/2\mathbf{E}(\mathbf{x},t)\exp -i\omega_p t + c.c.$, where the rapid time dependence at the local plasma frequency, $\omega_p = (4\pi e^2 n_0 / m_e)^{1/2}$ ,has been separated out. Here $n_0$ is the background electron density which may be slowly varying in space. The envelope $\mathbf{E}$ obeys

$$\nabla \bullet \left[ 2i\omega_p(\partial_t + \nu_e *) + 3v_e^2\nabla^2 - \frac{4\pi e^2}{m_e} n \right] \mathbf{E} = 2i\omega_p \nabla \bullet \mathbf{J_{ext}} \quad . \quad (1)$$

where $v_e^2 = T_e / m_e$ and $n(\mathbf{x},t)$is the fluctuation of the electron density about $n_0$. The current $\mathbf{J_{ext}}$ describes the coupling of the Langmuir field to the radiation field(s) including the driver or "pump" field. The explicit forms of $\mathbf{J_{ext}}$ are given below and depend on the instability being considered. The damping operator $\nu_e *$ is nonlocal in real space but local in k space where $\nu_e(k) = \nu_{ec} + \nu_{Landau}(k)$ with $\nu_{ec}$ ($\nu_{ec} = 1/2\nu_{ei}$) the collisional damping and $\nu_{Landau}(k)$ is the Landau damping. Provided $n / n_0 << 1$ and $ZT_e >> T_i$ the equation for $n(\mathbf{x},t)$ is

$$\left(\partial_t^2 + 2\nu_i * \partial_t - c_s^2\nabla^2\right) n = n_0 c_s^2 \nabla^2 (U / T_e) \quad (2)$$

where $\nu_i$ is the ion acoustic Landau damping which is local in k space and $c_s = \sqrt{ZT_e/m_i}$ is the ion sound speed. $U$ is the ponderomotive potential of the high frequency fields:

$$U = \sum_j \left|\mathbf{E_j}\right|^2 \frac{\omega_p^2}{\omega_j^2 16\pi n_0 T_e} \quad (3)$$

where the $\mathbf{E}_j$ are the envelopes ( discussed below) of the high frequency fields. More details concerning these models can be found in the references [5,6] and references therein.

Equations (1) and (2) have the form of driven, damped, Zakharov [7] equations. Modifications of (2) to take more accurate account of the ion acoustic response when $ZT_e \approx T_i$ have been given in [5] and [8]. In some

cases, especially when stimulated Brillouin and filamentation are important, further hydrodynamic nonlinearities must be included in (2).

These model eqution have been solved using several numerical techniques. The most common methods are split step, pseudo spectral methods, in which the evolution of the linear operators is conducted in k space while the nonlinear terms are evaluated in real space. More details are found in the references.

How accurate are the reduced descriptions compared to the "exact " Vlasov theory? The reduced models have the apparent advantage of only needing to treat the evolution on the slow "ion time scale" allowing for more feasible long time simulations, However collisionless heating and hot electron acceleration, which arise out of the Landau damping, imply the evolution of the background velocity distribution functions which in turn determine the Landau damping. This evolution is often not treated adequately by the reduced models and limits their accuracy on the time scales of this kinetic evolution. Some aspects of this problem have been studied in the critical density regime by J.G.Wang et al [9]. When collisionless heating effects are suppressed, say by letting the hot electrons leave the system be replaced by thermal electrons, good agreement between the Vlasov simulations and the reduced models is obtained. We recently proposed a new "local quasilinear theory" which transforms the kinetic theory to the slow time scale[5]. In this theory the evolution of the spatially averaged velocity distribution function is described by the usual quasilinear equation. However the theory also treats the spatially localized distortions of the distribution functions, as clearly seen in the Vlasov simulations, associated with the burnout of collapsing cavitons by hot elecron acceleration. We are presently attempting to see if this kinetic evolution can be incorporated in our simulation codes.

The reduced models have another advantage that collisional damping of Langmuir waves and related thermal noise sources can easily be treated. Collisional damping is not easy to include in Vlasov or particle -in- cell (PIC) simulations. PIC simulations usually also introduce unphysically high noise levels which can distort the results for weakly driven systems. In my opinion the use of PIC simulations, for the problems discussed in this paper, has yet to be fully exploited, particularly using the new highly parallel computing architectures. Roughly speaking, the PIC codes, as they have been historically used, are complementary to the reduced model codes. The former being used for strongly driven systems for short times. The reduced models are limited to weakness conditions such as

$|\mathbf{E}|^2 / 4\pi n_0 T_e << 1$ and $n / n_0 << 1$. Recently[10] we carried out a PIC simulation of a strongly driven 1D capacitor model of resonance absorption for which the early time Langmuir fields had $|\mathbf{E}|^2 / 4\pi n_0 T_e >> 1$. Because of strong collisionless heating, which raised $T_e$, the system quickly evolved to $|\mathbf{E}|^2 / 4\pi n_0 T_e << 1$ in a state of Langmuir turbulence where the reduced description was again applicable.

Experience has shown that physical effects common to all three instabilities arise in the reduced model simulations:

1.) The parametric excitation of the *primary* Langmuir waves (LWs) at $\mathbf{k}_1$ and the other daughter waves arising from the linear parametric instabilities. (A check of the linear theory is always carried out in our simulations.) For all these instablities there is a fundamental (homogeneous, convective) growth rate parameter $\gamma_0$ which depends on plasma conditions and pump intensity[11]. The damping threshold for convective growth is determined by $\gamma_0^2 = \gamma_1\gamma_2$ , the product of the daughter wave damping rates.
2.) Secondary Langmuir decay of the primary LWs into another LW and an ion acoustic wave (IAW): LW->LW'+IAW. This leads to a transfer of LW energy to lower k. It is most prominent at the lower density ranges allowed for a given instability , e.g. see [12].
3.) The product of the LW damping and the IAW damping determines the threshold for the secondary decay.In many cases of interest the LW collisional damping dominates here. This damping threshold can be the control valve determining the ultimate saturation level. This is illustrated for SRS in Section 4.
4.)Langmuir collapse: Langmuir fields selfconsistently trapped in a collapsing density cavity (a caviton). The collapse to smaller dimensions results in a transfer of LW energy to higher k. This process dominates in the higher density ranges allowed for a given instability.
5.) Pump depletion saturation is usually important only for very strong driving and /or for systems many gain lengths long.
6.) Collisionless (Landau) damping of LWs arrests the collapse at scales of 10-15 $\lambda_{De}$ and generates hot electrons.
7.) Saturated LW ampltudes are well below wavebreaking levels for many cases of practical interest including the experiments discussed below.
8.) High levels of IAW fluctuations are generated by ponderomotive effects: Secondary decay and Langmuir collapse.

9.) The high levels of IAWs thus generated can have a significant effect on SBS: Long wavelength IAWs ($k << 2k_0$) can detune SBS[13] while IAWs with $k \approx 2k_0$ can act as a super thermal seed for SBS [14,15,16].
10.) When (as is usually the case) the instability region is spatially localized, the averaged ponderomotive pressure of the induced LW electric fields in this region , which is a function of the pump intensity, is usually much stronger than the ponderomotive pressure of the pump wave itself. This has important implictions for density profile modification and filamentation [17].

In the following Sections I will try to illustrate these points using sample results from simulations of the three instabilities. Space does not permit a comprehensive investigation of any of these nor a complete listing of important references. More details futher references are found in the cited references. In Section 2 the IAD and the related modulational instability near critical density for the pump wave is treated. Comparison with Thomson scatter radar spectra obtained by Sulzer and Fejer[18] during RF ionospheric modification has provided beautiful confirmation of the predicted Langmuir collapse signatures. Section 3 treats the TPD and successful comparison is made with the Thomson scatter and $3/2\omega_0$ data of Meyer and Zhu[19]. Section 4 is devoted to SRS for which Baker et al [20] have recently observed the Thomson scatter signature of the secondary Langmuir decay wave. Scaling laws of relevance to certain ICF applications arise out of a local "mesoscale" analysis of the saturation [12].

## 2.Near critical density instablities: The ion acoustic decay and modulational instabilities.

For this density regime we can usually take $k_0 = 0$ so that the pump representation, the pump coupling current and ponderomotve pressure for Eqns.(1) and (2) are

$$2i\omega_p \mathbf{J_{ext}} = \frac{4\pi e^2}{m_e} n\mathbf{E_0} \quad , \qquad \mathbf{E_0}(\mathbf{x},t) = \mathbf{E_0} e^{-i\Omega_1 t} \tag{4}$$

$$U = \left|\mathbf{E}(\mathbf{x},t) + \mathbf{E_0}\right|^2 / 16\pi n_0 T_e \ , \qquad \Omega_1 = \omega_0 - \omega_p$$

The control parameter for the density is the frequency mismatch $\Omega_1$ $(|\Omega_1| << \omega_p)$.

Thomson scatter measurements of the turbulence induced in the F-layer of the ionosphere by powerful radio waves are in detailed agreement with predictions in the collapse regime. The first identification of the collapse

signatures was made by Cheung et al [21] based on the predictions of [22]. It was subsequently realized that these signatures had been observed earlier by Djuth et al [23] but not physically identified. Because the collapse ideas were regarded as controversial a great deal of experimental effort was devoted to test these notions. This work culminated in the beautiful experiments by Sulzer and Fejer[18] which achieved altitude resolution of 150m and temporal resolution of 10 micro seconds for the Thomson scatter power spectra for fluctuations at the single k vector probed by the radar. The model predicts that the strongest turbulence in a smooth ionosphere will be at the highest heater standing wave maximum. (Recall that the heater wave is reflected at critical density). The predicted power spectra at various k values close to those probed by the Arecibo radar are shown in Fig 1 taken from [5]. The dotted line is the pump frequency which was 5.1 Mhz for the experiments.. The broad spectrum with frequencies lower than the pump frequency is from caviton collapse. The instantaneous eigenfrequencies of the trapped Langmuir field in the caviton during collapse sweep over a range of frequencies below the local plasma frequency ( zero frequency in the figure). The high frequency peak results from free LWs emitted during collapse.

In many of the figures of this paper results are presented in scaled units: Electric fields in units of $(64\pi\eta n_0 T_e / 3M)^{1/2}$, lengths in units of $3/2M^{1/2}\lambda_D$, time in units of $3/2M\omega_p^{-1}$, and densities in units of $4/3n_0M^{-1}$, where $M = m_i / \eta m_e$ and $\eta \equiv c_s^2 / (T_e / m_i)$ .

Altitude resolved spectra from Sulzer and Fejer are shown in Figure 2. The first set of spectra are shown just after the turn on of the RF pump *in an unpreconditioned ionosphere.* A weak signal is observed at the so called matching height where the radar can detect a LW excited by the IAD instability. At 3 ms after turn on the broad caviton and free LW spectral features are observed at the altitude of the strongest HF E field as predicted. At 11ms, which is 1 ms after the turn-off of the pump, the caviton feature, which exists only in the presence of the pump, has rapidly decayed as predicted because of strong transit time damping of the collapsing cavitons, and only the free LWs which are natural oscillations of the undriven plasma persist (for a collsional damping time) and lie along the radar observed dispersion curve. This is all in perfect agreement with the strong Langmuir turbulence scenario predicted by the reduced model but totally at odds with the weak turbulence predictions of Langmuir decay cascades. Many more details are given in the cited references.

In the observations mentioned above the heater beam was on for 5ms. and off for 950ms. and this pattern was repeated for many cycles.When the heating time is a larger fraction of the 1s. period or when the pump is turned on in a preconditioned (previously heated) ionosphere the situation is more complex, signatures of secondary decay cascades appear at lower altitudes but above where they should be in the unperturbed ionospheric density profile. It is certain that persistent density irregularities are induced on these longer time scales by the induced turbulence itself. One effect which we are investigating [17] is the depletion of density by the ponderomotive pressure of the induced turbulence at the heater wave standing wave maxima. This forms a half-wavelength density depletion grating which inhibits the propagation of the pump to higher altitudes. The induced turbulence then decays at these higher altitudes allowing the pump to again propagate and the process repeats itself in a quasi periodic fashion with a period of about 50 ms for typical conditions. It is also known that geomagnetic field aligned density irregularities form on this same time scale but the theory for this is less well developed.

For the IAD induced by lasers a different regime is possible for which the LW collisional damping exceeds the daughter IAW frequency- $\nu_{ec} \geq k_1 c_s$. This was the subject of a recent collaboration [24]. In Figure 3 we compare this case with the ionospheric case where $\nu_{ec} << k_1 c_s$ in a density regime where the saturation by secondary decay is the dominant process. In the ionosphere case the modal energy distribution for LWs and IAWs shows the "onion skin" distribution in k space resulting from several steps of a Langmuir decay cascade. For any single k in this spectrum the frequency spectrum $|\mathbf{E}(\mathbf{k},\omega)|^2$ has a sharp peak at the free LW frequency corresponding to the value of k. In contrast in the laser case mentioned above the modal energy distribution has no obvious cascade structure but the *frequency spectrum* for a given k does! This can be understood by remembering that when $\nu_{ec} \geq k_1 c_s$ the IAD antiStokes mode is strongly coupled to the pump and Stokes mode raising the threshold [25]. The saturation scenario is completely changed by the linear excitation of the antiStokes mode. Details are given in [24].

## 3. The two plasmon decay instability at quarter critcal density.

Recently Meyer and Zhu [19] have used Thomson scattering to measure the distribution of Langmuir density fluctuations in k space. Meyer's group has also measured the angular distribution and power spectra of radiation emitted at frequencies near $3/2\omega_0$ The TPD was driven in a long

scalelength ( 1-2 mm) Nitrogen plasma by an f/7, near-diffraction- limited, C02 laser. This is a nearly ideal experiment against which to test the reduced model predictions. Cobble et al [26] have recently observed $3/2\omega_0$radiation in indirect drive NIF-plasma emulation experiments performed on NOVA. It is expected that direct drive targets for the NIF will have greater scale lengths near quarter critical density and be more susceptible to TPD [27]. Peyser et al [28], using induced spectral incoherence (ISI), and Seka et al [29], using smoothing by spectral dispersion (SSD), have studied the effect of these beam smoothing techniques on suppressing TPD. They observed that significantly more laser band width is required to suppress TPD than required to suppress SRS or SBS.

The linear theory of TPD in a homogeneous plasma has ben known since the 1966 work of Goldman [2]. The most detailed estimates of the thresholds in an inhomogeneous plasma [30] show that for the density scale lengths in the experiments of Meyer et al the homogeneous damping threshold exceeds the gradient threshold. The condition for the maximum TPD growth rate, and the wave vector and frequency matching conditions imply that the daughter Langmuir waves with the highest growth rate have wave vectors in the x,y plane which obey the equations:

$$\begin{aligned} (k_y - k_0)^2 - k_x^2 &= 1/4k_0^2 \\ \Omega_2 &= (3/2\omega_p)[2(k_x^2 + k_y^2) + k_0^2 - 2k_0k_y]\lambda_D^2 \end{aligned} \tag{5}$$

were we take $\mathbf{k_0}$ to be in the y direction. The threshold value of $|\mathbf{E}_0|$ which we call $E_T$ is determined by the LW collisional damping is given by $k_0eE_T/(4m_e\omega_0) = \nu_e(k=0)$ The external coupling current and ponderomotive potential in Eqns. (1) and (2) for the TPD are [6,31,32]

$$\begin{aligned} 2i\omega_p\mathbf{J_{ext}} &= \frac{e}{4m_e}\left[\nabla(\mathbf{E}_0 \bullet \mathbf{E}^*) - \mathbf{E}_0(\nabla \bullet \mathbf{E}^*)\right] \\ U = |\mathbf{E}(\mathbf{x},t)|^2/16\pi n_0T_e \quad &; \quad \mathbf{E}_0(\mathbf{x},t) = \mathbf{E}_0e^{-i(\Omega_2 t - \mathbf{k_0}\bullet\mathbf{x})} \\ \Omega_2 &= \omega_0 - 2\omega_p \end{aligned} \tag{6}$$

The control parameter for the density is the frequency mismatch $\Omega_2$.The dipersion relation for light in a plasma with $\omega_0 \approx 2\omega_p$ gives $k_0 = |\mathbf{k_0}| = \sqrt{3/4}\omega_0/c$ to terms of order $\Omega_2/\omega_0$ which is always a small parameter; otherwise the density is so low that the primary LWs are strongly Landau damped and the TPD is below threshold.

The parameters for our simulations [32] were chosen to approximately match the known parameters of the Meyer and Zhu experiments: $k_0\lambda_{De} \cong \sqrt{3}\mathrm{v_e}/c = 0.05$ corresponding to $T_e = 0.4\mathrm{keV}$ and $\nu_e(0)/\omega_{pe} = \nu_{ei}/\omega_0 = 2.\times 10^{-4}$ corresponding to a N charge state Z=4 at this temperature and density. We have also taken $ZT_e/T_i \approx 10$, which is not known for the experiment, and which gives an ion acoustic damping to frequency ratio $\nu_i(k)/kc_s = 0.05$.

In Figure 4 we show contour plots taken from [32] of the distribution of Langmuir density fluctuations, $< k^2 \left|E(k_x,k_y)\right|^2 >$, and low frequency (IAW) density fluctuations, $< \left|n(k_x,k_y)\right|^2 >$, for two densities and two values of the pump intensity relative to the threshold $E_T$. For the weakest drive the two pairs of primary most unstable Langmuir modes are clearly seen in the spectra indicated by circles. Also seen, indicated by diamonds, are the LWs resulting from the secondary decay of the primary modes. ( The secondary decay modes are diagonally across the origin from the corresponding primary mode.) Both the primary and secondary modes are broadened into crescents because the nearby less unstable primary modes are also excited but more weakly. In this weak driving case the Langmuir energy flows to lower k consistent with the observations of Baldis and Walsh [33].The low frequency IAW spectrum also has outer crescents arising from the IAWs participating in the secondary decay processes. There are also low k structures which arise from the ponderomotive beats of nearby modes in the crescents of the Langmuir spectrum.

For stronger driving, especially at the higher density, the primary and secondary modes are nearly obscured by a broad background spectrum which spreads to higher k. We attribute this broad spectrum to Langmuir collapse. Baldis and Walsh [33] observed that the spectrum spread to higher k for stronger driving. The low k structures for stronger driving and higher densities also contain contributions from the density fluctuations resulting from collapsing cavitons.

The fact that no tertiary or higher Langmuir decay process is seen for TPD (in contrast to the case of IAD or SRS) appears to be due to the modification of the linear wave dispersion because of the parametric coupling induced by the coherent pump [6]. In a region of k space surrounding the most unstable mode the dispersion of the linear response is modified away from the usual LW dispersion, $\omega_\ell(\mathbf{k}_\ell) = \omega_p(1+3/2k_\ell^2\lambda_D^2)$,

even for k values for which the parametric waves are stable. This effect is especially strong because of the symmetry the TPD.

Early studies of TPD saturation by secondary Langmuir decay were carried out by Karttunen and Heikkenen [34]. They considered weak (zero) linear wave damping which would correspond to our parameter $E_0 / E_T \to \infty$.They also used a limited set of coupled free wave envelope equations describing a single secondary decay which cannot account for caviton collapse which we find to be important in strongly driven regimes.

The measure of caviton activity (which we use in all our simulations) is the correlator:

$$C_{n|\mathbf{E}|^2} = -\frac{< n|\mathbf{E}|^2 >}{< n^2 >^{1/2} < |\mathbf{E}|^2 >} \tag{7}$$

Because a caviton consists of a localized peak in $|\mathbf{E}|^2$ on top of a density depression ($n < 0$) this correlator will be relatively large and positive at the location of a caviton but will be small and of undeterminate sign for linear waves. The angular brackets indicate a spatial and temporal average. In Figure 5 this correlator is plotted versus density for several pump strengths. We see that the caviton activity is strongest at the highest densities approaching $0.25 n_c$ and increases with pump strength at every density.

The most commonly used diagnostic of TPD activity is the secondary radiation at $3/2\omega_0$. This radiation is produced by the transverse part of the current [6]

$$\mathbf{J}_{3/2} = -\frac{e}{16\pi i m_e}(\nabla \bullet \mathbf{E})\mathbf{E}_0 \tag{8}$$

This current involves the beating of the high freqency Langmuir density oscillations with the pump field. Since the radiation must satisfy the dipersion relation $(3/2\omega_0)^2 = \omega_p^2 + k_{3/2}^2 c^2$ it follows (remembering that $k_0 \approx \sqrt{3/4}\omega_0 / c$) that $|\mathbf{k}_{3/2}| \equiv k_{3/2} \cong \sqrt{2}\omega_0 / c \approx \sqrt{8/3}k_0$ to terms of order $\Omega_2 / \omega_0$ which is a small parameter for this problem. The following wave vector and frequency matching conditions must be satisfied in this process:

$$\mathbf{k}_{3/2} = \mathbf{k}_0 + \mathbf{k}_\ell, \quad \omega_{3/2} = \omega_0 + \omega_\ell(\mathbf{k}_\ell) \tag{9}$$

It is easy to show that these conditions imply for free LWs:

$$\begin{aligned} k_\ell^2(\theta)/k_0^2 &= 11/3 - \sqrt{8/3}\cos\theta \\ \omega_{3/2} - 3/2\omega_0 &= -1/2(\omega_0 - 2\omega_p) + 3/2(k_\ell^2\lambda_D^2) \end{aligned} \tag{10}$$

The first condition says that the Langmuir wave vector must lie on the "radiation circle" which are the dotted circles show in Figure 4. Here $\theta$ is the angle between the direction of the 3/2 emission, $\mathbf{k}_{3/2}$, and $\mathbf{k}_0$. The intensity of 3/2 emission is proportional to its Poynting flux which is to a good approximation proportional to $\left|\mathbf{J}_{3/2}(\mathbf{k}_{3/2},\omega_{3/2})\right|^2 - \left|\mathbf{k}_{3/2}\bullet\mathbf{J}_{3/2}(\mathbf{k}_{3/2},\omega_{3/2})k_{3/2}^{-1}\right|^2$.The contours of this emission are plotted in Figure 6 for two values of $n_0 / n_c$ and two values of the pump strength. At $n_0 / n_c$=0.244 the radiation is in a forward lobe. This is consistent with the intersection of the the radiation circle in Fig.4 for this density with the secondary decay LWs. Note that the primary LWs do not contribute to the radiation! For stronger driving the LW spectrum broadens and the radiation pattern does likewise and a weaker backward emission lobe appears. For $n_0 / n_c$=0.234 the emission is in a backward lobe which fills in with stronger driving. In this case again it is the secondary decay modes in the backward direction which couple to the 3/2 light and not the primary unstable modes. The computed frequency spectra in the directions of strongest emission in Figure 6 are plotted in Figure 7 for the same two densities. For the lower(higher) density the spectrum is red (blue) shifted from $3/2\omega_0$ The peaks in these spectra are close to the frequency determined from the second line of Eqn. (10). This formula predicts that for $(\omega_0 - 2\omega_p)/\omega_p < (>) 3/2(k_\ell\lambda_D)^2$ the emitted light will be blue (red) shifted with respect to $3/2\omega_0$. Thus for a *given* angle of emission lower densities favor red shifts. With stronger driving these frequency spectra also broaden. Broadening on the low frequency side where $\omega_{3/2} - 3/2\omega_0 \le -1/2(\omega_0 - 2\omega_p)$ is evidence of Langmuir collapse but this criterion is difficult to apply to experiments since it requires knowing the density of emission and the angle of emission.

The emission criteria (10) plus the fact that the secondary decay modes provide the emission lead to several other predictions [6] ,which we will not give here ,which are contrary to past theories which rely on coupling to the primary unstable modes. The only way the primary unstable modes can couple is if they propagate in a density gradient until they can satisfy the k matching condition [29]. Meyer [36] has shown that in typical cases the primary LWs will be collisionally damped before they can couple. Our nonlinear theory shows that coupling can occur *locally* through the secondary decay modes which is surely the strongest process in a long scale length plasma.

To make contact with the long scalelength experiments of Meyer et al [19,36] it is necessary to take into account the weak density inhomogeneity which we will take to be only in the direction of laser propagation ,$\mathbf{k_0}$, which is our y direction. If the macroscopic density variation is slow on the scale of the appropriate turbulence correltion length we can represent spectra as an incoherent sum over spectra at various densities calculated in homogeneous simulations at those densities. We call this a mesoscale method. To illustrate this consider the density power specrtum which determines the Thomson scatter signal.

$$<|n_e(\mathbf{k})|^2>=\int d^3x \int d^3x' \, e^{i\mathbf{k}\bullet(\mathbf{x}-\mathbf{x}')} <n_e(\mathbf{x})n_e(\mathbf{x}')> \qquad (11)$$

where the integration is over the whole observed volume.We can write the spatial correlation function in terms of relative and mean coordinates and assume that the system is translationally invariant in all but the y direction:

$$C(\frac{y+y'}{2},\mathbf{x}-\mathbf{x}')=<n_e(\mathbf{x})n_e(\mathbf{x}')> \qquad (12)$$

We can then Taylor expand the integrand around y'=y to obtain:

$$Volume\times\int dy\left[C(y,\mathbf{k})+i/2\frac{\partial}{\partial y}\frac{\partial}{\partial k_y}C(y,\mathbf{k})++\right] \qquad (13)$$

The second term in square brackets can be neglected if

$$(\frac{\partial}{\partial k_y}\frac{\partial}{\partial y}C(y,\mathbf{k}))/C(y,\mathbf{k})\approx \ell_c(\frac{\partial}{\partial y}C(y,\mathbf{k}))/C(y,\mathbf{k})<<1 \qquad (14)$$

Where the correlation length is $\ell_c \mp (\Delta k_y)^{-1}$if $\Delta k_y$ is the spectral width in the y direction. If the inhomogeneity is only in the density then we can convert to a density integration:

$$\int dyC(y,\mathbf{k})=\int dn_0(dn_0/dy)^{-1}C(\{n_0\},\mathbf{k}) \qquad (15)$$

But the spectrum at density $n_0$ , $C(\{n_0\},\mathbf{k})$ , can be calculated in a homogeneous simulation provided that the simulation cell has lengths larger than a correlation length. To compare with the experiments of Meyer et al [19,36] we have replaced the integral by a sum over 10 density values and have carried out the required 10 homogeneous simulations.The same procedure can be used to calculate the density averaged $3/2\omega_0$ radiation spectra which depend on a related correlation function.

The results of this incoherent density average are shown in Figures 8 and 9 which are to be compared to Figure 10 taken from Meyer and Zhu [19]. In Figure 8 we show a contour plot in k space of $<<k^2|\mathbf{E}(\mathbf{k})|^2>>$ which is proportional to the Langmuir density fluctuation spectrum.The double brackets indicate that this is a density average of the time averaged

spectrum in the saturated steady state. The inset in this figure shows the density profile that was chosen for the 10 density points to give the "best fit" discussed below. This figure is to be compared with Fig. 10a which is a contour plot of the Thomson scattering data by Meyer and Zhu. It is seen that the locations in k space of the most intense Langmuir activity agrees well with the calculations for $E_0 / E_T$=4. However the shapes of the contours differ. We believe, and J. Meyer agrees, that this is an artifact of the expermental data sampling. The theoretical spectra are based on about $10^4$ equally spaced points in the two dimensional k space whereas the data is collected along 15 discrete arcs in k space and the experimental contours are distorted by the geometry of the arcs. Better agreement is obtained for the angular distribution of the $3/2\omega_0$ radiation for which the density averaged spectra are shown in Figure 9. This turned out to be the most sensitive to the choice of the density profile which was chosen to give the best eyeball fit to the data shown in Figure 10b. Again the best agreement is found for $E_0 / E_T$=4. The theory matches the observed forward and backward emission lobes very well.It should be remarked that the angular positions of these lobes were not sensitively dependent on the density profile but their relative magnitudes were. The computed power spectra of the emission in the forward and backward lobes are also shown in Figure 9. These spectra are only in qualitative agreement with the observed spectra [36] ( which are not shown here.) In the forward direction the calculation shows a broad, probably collapse dominated, spectrum consistent with the fact that Meyer et al measured a spectrum broader than the band width of their spectrometer. In the backward direction we calculate a strong red shifted peak with a weaker, sharp, blue shifted peak whereas Meyer et al observe a distinct red shifted peak on a broad, partly blue shifted pedestal. The differences are probably due to the breakdown of the mesoscaling method in this case since the appropriate correlation length for this spectrum is very long for this regime. Nevertheless there is qualitative agreement with observations even in this case.

The best agreement with the observations is obtained for laser strengths in the range $4< E_0 / E_T<8$ Translated into intensities these are roughly a order of magnitude less than the putative averaged laser intensity. However, the TPD activity was observed for only 100ps during a 1ns pulse when the power was lower than the average power. Also convective losses of plasmons from the narrow beam, which will raise the effective threshold, where not taken into account in the theory.

## 4. Stimulated Raman Scattering.

SRS reflectivities in the 10%-20% range have recently been observed at NOVA using NIF emulation targets [37]. Only partial control was achieved using SSD beam smoothing. An understanding of the saturation mechanisms for SRS would be useful for the more efficient design of ICF targets. The saturation of SRS by secondary Langmuir decay has been studied by several authors [34]. Reduced model simulations in 1D have been published by Kolber et al [38] and Bezzerides et al [39] who showed that for weak laser intensities that this was the primary saturation mecanism. Recently Baker et al [20] have measured the backward going secondary LW and perhaps the tertiary forward going decay wave using Thomson scattering. A spectrum from their work is shown in Figure 11. For moderate drive Bezzerides et al [39] have shown that collapse plays a role in the saturation.

To treat the stimulated scattering instabilities we need in addition to (1) and (2) evolution equations for the incident and backscattered light. For the backscattered SRS light with electric vector $\mathbf{E}_R(\mathbf{x},t)e^{-i\omega_R t} + c.c.$, the envelope field obeys:

$$\left[2i\omega_R(\partial_t + \nu_R) - c^2\nabla^2 + \omega_p^2 - \omega_R^2\right]\mathbf{E}_R + (\omega_p^2 / n_0)[n\mathbf{E}_R]_T = (e / m_e)(\omega_R / \omega_0)\left[\mathbf{E}_0(\nabla \bullet \mathbf{E}^*)\right]_T e^{-i(\omega_0-\omega_R-\omega_p)t} \quad (16)$$

The subscript $T$ denotes the transverse component of the vector. A similar equation exists for the incident laser light and takes into account pump depletion. If we futher introduce the spatial envelope representation for the light fields $\mathbf{E}_R = \hat{\mathbf{E}}(\mathbf{x}_\perp,t)_R e^{-ik_R y}$, $\mathbf{E}_0 = \hat{\mathbf{E}}(\mathbf{x}_\perp,t)_0 e^{ik_0 y}$ , ,where the y coordinate is again along $\mathbf{k}_0$ and $-k_R$ is the backscattered light wave number in the opposite direction, we obtain the paraxial equation:

$$\left[2i\omega_R(\partial_t + \nu_R - \mathrm{v}_R\partial_x - c^2\nabla_\perp^2\right]\hat{\mathbf{E}}_R + (\omega_p^2 / n_0)[n\hat{\mathbf{E}}_R]_T = (e / m_e)(\omega_R / \omega_0)[\hat{\mathbf{E}}_0(\nabla \bullet \mathbf{E}^*)]_T e^{-i\delta\omega t} e^{i(k_0-k_R)x} \quad (17)$$

where $\delta\omega \equiv \omega_0 - \omega_R - \omega_p$ and $\mathrm{v}_R = k_R c^2 / \omega_R$ (Note the complete frequency mismatch which takes into account the thermal dispersion of LWs is $\Delta\omega = \delta\omega - (3/2)\omega_p(k_0 - k_R)^2\lambda_D^2$ ) These equations must be solved with the proper outgoing wave (or for the pump, ingoing wave) boundary conditions. The examples shown below where obtained with a 1D version of this code. A 2D version is now under development. It will be used to study such practical questions such as the behavior or SRS in the hot spots of a laser beam processed by a random phase plate and how the

hot spot statistics affect the onset of SRS. Such questions have recently been studied by Harvey Rose for the case of SBS [40].

The external source term in (1) for SRS is

$$S(\mathbf{x},t) = 2i\omega_p \nabla \bullet \mathbf{J}_{\mathbf{ext}} = (e/4m_e)\nabla^2(\hat{\mathbf{E}}_0 \bullet \hat{\mathbf{E}}_R^*)e^{-i\delta\omega t} \qquad (18)$$

For SRS we then have the basic growth rate $\gamma_0 = \sqrt{\omega_p^2/\omega_0\omega_R}|\mathbf{e_0} \bullet \mathbf{e}_R|(ek_1E_0/m_e\omega_0)$ where $\mathbf{e_0}, \mathbf{e_R}$ are unit vectors describing the polarization of the incident and scattered light, respectively. The simulations described below are in a finite length plasma and are driven above the absolute instability damping threshhold, $\gamma_{0T} = 2\sqrt{c/v_R}\nu_e(k=0)$, which determines an absolute threshold intensity $I_T = c|\mathbf{E}_{0T}|^2/8\pi$.

In Figure 12 are shown the results of a 1D simulation of SRS for a localized pumping region 45 laser wavelengths, $\lambda_0$, long which is a poor man's representation of a laser hot spot in 1D. The other physical parameters are $n/n_c = 0.2$, $T_e = 1kev$, $T_e/T_i = 2.4$, $Z = 4$, $A = 9$, for which $k_1\lambda_D = 0.125$ For these parameters $I_T = 2.0\times10^{14}$ W/cm$^2$. In Figure 12, $I/I_T$=2.27. The panels a, b, and c show the backscattered light field, $E_R(x,t)$, the induced density fluctuations, $n(x,t)$, and the modulus, $|E(x,t)|^2$, of the induced Langmuir field at a time 70 in scaled units corresponding to about 150ps. In panel d the time averaged modal spectrum, $<|E(k)|^2>$ , shows the primary unstable LW at $k = k_1 = 9$ and the secondary decay LW at and in panel e the spectrum, $<|n(k)|^2>$, shows the corresponding decay ion acoustic waves at $k \cong \pm(2k_1 + k_*) = \pm19$.
The quantities are time averaged over many laser cycles.These quantities grow spatially in the direction opposite to the laser propagation ,which is to the right, as expected from the linear theory. The averaged reflectivity in this case was only X%.Also shown are the spectral densities of IAWs in k space, which clearly show the secondary peaks associated with the decay IAWs. Kolber et al [38] obtained similar results.

Results for the same plasma parameters but for a pumping region half as long and with a stronger drive $I/I_T = 64$ are shown in Figure 13 taken from [39]. Spatial plots are shown of the scattered light reflectivity (R) in arbitrary units, the density fluctuation $<\delta n(x,t)>/n_0$, and the energy density of the Langmuir field,$<|E(x)|^2>/16\pi n_0T_e$ are shown.The

maximum reflectivity in this case was 1.2%. The modal energy spectrum in this case does not show sharp secondary (and higher order) decay features as found for weaker drive but has a peak at $k_1$ on a broadened spectrum. This case is in the collapse regime.

The "daughter wave" part of the Langmuir spectrum which couples directly to the laser pump are the modes in the spectral peak near $k = k_1$ [39]. A field $E_1(x,t)$ is calculated using only those modes in $,\Delta k$, the FWHM of this peak. If the daughter wave intensity, $|E_1|^2/4\pi n_0 T_e$, exceeds a threshold intensity $E_T^2/4\pi n_0 T_e = 16[\nu_e(k_1')/\omega_p][\nu_i/\omega_i]$ , then the daughter wave at $k_1$ can decay into another LW at $k_1'$ and an IAW at $k_2'$ ;$(\mathbf{k}_1 = \mathbf{k}_{1'} + \mathbf{k}_{2'})$, provided that $3k_1\Delta k v_e^2 < \nu_e(k_1')\omega_p$. In Figure 12 the ratio $<|E_1(x,t)|^2>/E_T^2$ is also plotted and we see that the secondary decay threshold is exceeded throughout the system.

The Langmuir field in (1) is driven by the source term S(x,t) given by (18). In Figure (13) we have plotted the time averaged modulus of the daughter wave field, $<|E_1(x,t)|^2>/E_T^2$, versus the time averaged source term $<|S(x,t)|^2>^{1/2}/S_T$ which we have normalized by $S_T = 2\omega_p E_T \nu_e(k_1)$ which is the source strength which would lead to $E_T$ in the *linear* response of E. These curves, obtained from *global* simulations [39], are shown for a range of values of $I$, $L$, and $\nu_{ei}$ over which there is a wide range in the magnitudes of $<|E_1|^2>$ and $<|S|^2>$. The fact that all these curves lie remarkably close to one another suggests that there is a nearly universal behavior in the relationship between these scaled, local quantities. We have also plotted the same quantities calculated in a homogeneous simulation (periodic boundary conditions) driven by a *specified* source. The closeness of this curve to the others indicates that a local, mesoscale analysis can be a reasonable approximation to the full, self-consistent , global simulation. A fair fit to the data in Figure 13 is given by

$$<|E_1|^2>/E_T^2 = (<|S|^2>/S_T^2)^{1/\eta} \quad ; \quad 3.2 < \eta < 3.5 \qquad .(19)$$

We introduce the coarse grained average fields: $\overline{E}(x,t) \equiv \int_{-\ell_c/2}^{\ell_c/2} d\zeta E(x+\zeta,t)$

where $\ell_c \approx (\Delta k)^{-1}$. Applying this to (11), assuming a quasi steady state to neglect light transients, assuming exact frequency matching $(\Delta\omega = 0)$,

neglecting pump depletion, and writing the fields as $E_R = |E_R| e^{i\phi_R}$ , $E_0 = |E_0| e^{i\phi_0}$ , $E = |E| e^{i\phi_E}$ we come to the equation

$$-v_R(\partial / \partial x)|\overline{E}_R| \propto |E_0|\,|\overline{E(x)e^{-ik_1 x}}| \tag{20}$$

where we have assumed phase matching $\phi_0 = \phi_R + \phi_E$. It follows from the definition of the daughter field that $|\overline{E(x)e^{-ik_1 x}}| = |E_1(x)|$. Now if we replace $|E_1(x)|$ by its local rms value and approximate this by the numerically obtained scaling formula (19), and remember that $|S| \propto |E_0|\,|E_R|$, we obtain:

$$(d / dx)|E_R|^{1-1/\eta} \propto |E_0|^{1+1/\eta} E_T^{1-1/\eta} \nu_e^{-1/\eta} \tag{21}$$

which is easily integrated to obtain the scaling of the reflectivity:

$$\mathrm{R} \propto \frac{|E_R|^2}{|E_0|^2} \propto \nu_i \nu_e^{\left(\frac{\eta-3}{\eta-1}\right)} I^{\left(\frac{2}{\eta-1}\right)} L^{\left(\frac{2\eta}{\eta-1}\right)} \tag{22}$$

where we have used the definitions of $S_T$ and $E_T$ and $L$ is the length of the active region of integration. An important result, which is independent of the exact numerical scaling law, and which is verified by the simulations, is that the reflectivity is proportional to the IAW damping , $\nu_i$. Recent experiments by Kirkwood et al [37] using "gas bag" NIF emulation targets at NOVA have measured such an increase of SRS reflectivity along with an expected decrease of SBS reflectivity with IAW damping. In these experiments the IAW damping was varied by varying the hydrogen content of the laser produced plasma. We see that R is weakly dependent on the LW damping , $\nu_e$, (provided L does not depend on it [39]) and scales roughly like $IL^2$. Kolber et al [38] obtained the scaling of Eqn. (22) with $\eta = 3.0$. The reflectivity scaling laws are in good agreement with the numerical simulations [39] but the numerical values (obtained by inserting factors suppressed in the formulas above) can differ from the simulations by factors as large as 3. We attribute this to nonlocal and phase dependent effects on the light propagation [39].

## 5. Summary and conclusions.

It appears then that reduced models have had some success in reproducing and predicting experimental observations. They are an efficient and

flexible tool which in some cases are superior to or complementary to full kinetic simulations.

The inclusion of collisionless heating effects in these reduced models is an outstanding and largely unsolved problem which limits their usefullness in some regimes. To study hot electron production in laser driven ICF plasmas or in ionospheric modification experiments (and the resulting air glow) a better treatment of these kinetic effects is essential.

There are several practical applications important for ICF plasmas which remain to be carried out. These include the treatment of realistic laser beam hot spot geometries and statistics which arise when random phase plates process the beams. This is really the only situation, for short wave length lasers, where the laser beam properties can be well characterized [40]. The effect of temporal beam smoothing should also be studied. More work on inhomogeneous plasmas, both long scale length cases where local mesoscale methods can be used and short scale length cases where direct simulation is possible, is needed. The coupling of the instabilies, e.g. SBS with TPD and SRS or the hybrid TPD-SRS instability very close to 1/4 critical density is largely unexplored in the nonlinear regime.

The modification of the density profile due to the ponderomotive or thermal pressure of the induced Langmuir turbulence has important implications for both laser and ionospheric experiments. For example in a region of strong Langmuir turbulence laser beam filamentation can be significantly enhanced.

**Acknowledgements:**

We wish to thank M. Sulzer, J. Meyer, J. Cobble, J. Fernandez, R. Kirkwood, B. MacGowan, and K. Baker for providing figures and information concerning their exoeriments.

## References


[1] DuBois, D.F., and M.V.Goldman, Phys. Rev. Lett. **14**,544 (1965): Phys. Rev. **164**, 207 (1967) and Silin, V.P.,Sov. Phys. JETP, Engl. Transl., **21**, 1127 (1965).

[2] Goldman,M.V., Ann. Phys. (N.Y.) **38**, 117 (1966).

[3] Goldman, M.V., and D.F. DuBois, Phys. Fluids **8**, 1404, (1965).

[4] Baym, G., and R.W. Hellwarth, IEEE J. Quantum Electron.**1**,309,(1965).

[5] DuBois,D.F., D. Russell, and H.A.Rose, Phys. Plasmas **2**, 76, (1995).

[6] DuBois,D.F., D. Russell, and H.A.Rose, in preparation 1995.

[7] Zakharov, V. E.,Sov. Phys. JETP, Engl. Transl.,**35**, 908, (1972).

8] Goldman,M.V., D.L. Newman, and F.W. Perkins, Phys. Rev. Lett. **70**, 647, (1993).

[9] Wang,J.G., G.L. Payne, D.F. DuBois, and H.A. Rose, Phys. Plasmas **1**, 2531, (1994) and **2**, 1129, (1995) and to be published 1995.

[10] Gavrilov,E.M., D.F. DuBois, H.A. Rose, and A.M. Rubenchik, Phys. Plasmas **2**, 1907 (1995).

[11] Kruer, W.L., The Physics of Laser Plasma Interactions (Addison-Wesley, New York, 1988).

[12] DuBois,D.F., A. Hanssen, H.A.Rose,and D. Russell, J. Geophys. Res. **95**, 21221, (1990) and **97**, 17543, (1993).

[13] Maximov, A., W. Rozmus, V.T. Tikhonchuk, D.F. DuBois, H.A. Rose and A.M. Rubenchik, Submitted 1995.

[14 Rose ,H.A., D.F. DuBois and B.Bezzerides, Phys. Rev. Lett. **58**, 2547, (1987).

[15] Villeneuve, D.M., H.A. Baldis , and C.J. Walsh, Phys. Rev. Lett. **59**, 1585 (1987).

[16] Tanaka, K.A., B. Boswell, R.S. Craxton, L.M. Goldman, F. Gugiiemi, W. Seka, R.W. Short, and J.M. Soures, Phys. Fluids**28**, 2910, (1985) and,
Young, P.E., K.G. Estabrook, W.L. Kruer, E.A. Williams, P.J. Wegner, H.A. Baldis, and T.W. Johnston, Phys. Fluids**B 2**, 1907 (1990).

[17] DuBois, D.F., H.A. Rose, and A. Hanssen,in preparation.(1995).

[18] Sulzer, M.P., and J.A. Fejer, J. Geophys. Res. **99**, 15035 (1994).

[19] Meyer, J., and Y. Zhu, Phys. Rev. Lett. **71**, 2915 (1993).

[20] Baker, K.L., R.P. Drake, B.S. Bauer, K.G. Estabrook, and A.M. Rubenchick. Submitted 1995.

[21] Cheung,P.Y., A.Y. Wong, T. Tanikawa, J. Santoru, D.F. DuBois, H.A. Rose, and D. Russell, Phys. Rev. Lett.**66**, 2676 (1989).
[22] DuBois, D.F., H.A. Rose and D. Russell, Phys. Rev. Lett. **60**, 581, (1988).

[23] Djuth, F.T.,C.A. Gonzales, and H.M. Ierkic, J. Geophys. Res.**91**, 12089 (1986).

[24] Goldman, M.V., D.L. Newman, D. Russell, D.F. DuBois, H.A. Rose, R.P. Drake and A.M. Rubenchik Phys. Plasmas **2**, 1947 (1995).

[25] DuBois, D.F., and M.V. Goldman Phys. Rev. Lett. **19**, 1105 (1967).

[26] Cobble , J., private communication.

[27] Seka, W., B.B. Afeyan, R. Boni, L.M. Goldman, R.W. Short, K. Tanaka, and T.W. Johnston, Phys. Fluids **28**, 2570 (1985).

[28] Peyser, T.A., C.K. Manka, S.P. Obenchain, and K.J. Kearney., Phys. Fluids **B3**, 1479 (1991).

[29] Seka, W., R.E. Bahr, R.W. Short, A. Simon, R.S. Craxton, D.S. Montgomery, and A.M. Rubenchik, Phys. Fluids **B4**, 2233 (1992).

[30] Simon, A.R., R.W. Short, E.A. Williams, and T. Devandre, Phys. Fluids **26**, 3107, (1983).
[31] Sagdeev, R.Z., G.I. Solov'ev, V.D. Shapiro, V.I. Schevchenko,, and I.V. Yusupov, Sov. Phys. JETP **55**, 74, (1982).

[32] DuBois, D.F.. D. Russell, and H.A. Rose, Phys. Rev. Lett. **74**, 3983 (1995).

[33] Baldis,.H.A., and C.J. Walsh Phys. Rev. Lett. **47**, 1658 (1981).

[34] Karttunen, S.J., Phys. Rev. **A 23**, 2006 (1980) and Heikkinen, J.A., and S.H. Karttunen, Phys. Fluids **29**, 1291 (1986).

[35] Meyer, J., Phys. Fluids **B4**, 2934 (1992).

[36] Meyer, J., Y. Zhu, and F.L. Curzon, Phys. Fluids **B1**, 650 (1989).

[37] Kirkwood, R. and B. Mac Gowan, private communication.
[
[38] Kolber,T., W. Rozmus, and V.T. Tikhonchuk, Phys. Fluids **B5**, 138 (1993).

[39] Bezzerides, B., D.F. DuBois, and H.A. Rose, Phys. Rev. Lett. **70**, 2569 (1993).

[40] Rose, H.A. and D.F. DuBois , Phys. Rev. Lett. **72**, 2883 (1994)

**Figure Captions:**

Figure 1. Predicted Thomson scatter power spectra at a density close to that of the highest heater standing wave maximum for k values close to that observed by the Arecibo 430Mhz radar (from[5]). The dominant instablity in this regime is the purely growing modulational instability.

Figure 2. From Sulzer and Fejer[18]: Thomson scatter radar power spectra a a function of height at three times following the turn on of the heater in a quiet ionosphere.

Figure 3. Comparison of time averaged modal spectra, $<|\mathbf{E}(\mathbf{k})|^2>$, and power spectra, $<|\mathbf{E}(\mathbf{k},\omega)|^2>$, for $\nu_e(0) << k_1 c_s$ (left hand panels) and for $\nu_e(0) \approx k_1 c_s$ (right hand panels) From [8].

Figure 4. Modal spectra $<k^2|\mathbf{E}(\mathbf{k})|^2>$ and $<|n(\mathbf{k})|^2>$ for the TPD instablity in a homogeneous plasma for two values of $n_0 / n_c$ and two values of $E_0 / E_T$. The parameters for the simulation are given in the text.

Figure 5. The caviton correlator, $C_{n|E|^2}$, for the TPD as a function $n_0 / n_c$ of for three values of $E_0 / E_T$. For the same plasma parameters as Fig. 5.

Figure 6. Polar plots of $<|\mathbf{J}_{3/2}(k_{3/2},\theta)|^2>$ , time averaged, giving the $3/2\omega_0$ radiation patterns from TPD excited turbulence in a homogeneous plasma for two values of $n_0 / n_c$ and two values of $E_0 / E_T$. For the plasma parameters parameters of Fig. 4.

Figure 7. Power spectra of the $3/2\omega_0$ radiation ,$<|\mathbf{J}_{3/2}(k_{3/2},\theta,\omega)|^2>$, for the angles of maximum emission in Fig.6. Zero frequency corresponds to $3/2\omega_0$.

Figure 8. Time and density averaged modal spectra ,$<<|k^2\mathbf{E}(\mathbf{k})|^2>>$, calculated using the mesoscale method. the density profile for the 10 density average is shown in the inset; $n_0(y) / n_c$ on [0,2,0.25] versus $y / L$ on.[0,1] Except for $n_0 / n_c$ the parameters are the same as for Fig.4.

Figure 9. Time and density averaged angular distribution of $3/2\omega_0$ radiation and power spectra at angles of maximum emission for of Fig. 8.

Figure 10. From Meyer and Zhu[19], Fig. 5 : a. Contours of the saturated TPD wave intensity in k space obtained from streak records ot the

Thomson sactter spectra averaged over the first 100ps. of the laser pulse. The dashed line is the radiation circle. b. Angular distribution of emitted $3/2\omega_0$ intensity.

Figure 11. Thomson scatter spectrum of SRS langmuir waves from Baker et al [20] showing the SRS (our primary) LW, the LDI (our secondary) LW and the possible secondary (our teriary LW) decay feature.

Figure 12. Results of 1D reduced model simulations of SRS in a localized hot spot laser field whose envelope is shown by the dashed line in b. and c.. For the parameters given in the text with $I/I_T$=2.27. The panels a, b, and c show the backscattered light field, $E_R(x,t)$, the induced density fluctuations, $n(x,t)$, and the modulus, $|E(x,t)|^2$, of the induced Langmuir field at a time 70 in scaled units corresponding to about 150ps. In panel d the time averaged modal spectrum, $<|E(k)|^2>$ , shows the primary unstable LW at $k=k_1=9$ and the secondary decay LW at $k\cong -8$and in panel e the spectrum, $<|n(k)|^2>$, shows the corresponding decay ion acoustic waves at $k\cong\pm(2k_1+k_*)=\pm 19$ .

Figure 13. From [39]: a. The parameters are the same as for Fig. 12 except for $I/I_T$=64 and $L/\lambda_0$=22.5. Time averaged (over many laser cycles) spatial profiles of the excited Langmuir energy $<|E(x)|^2>/16\pi n_0T_e$ (solid line), the fractional density modulation $<\delta n(x)>/n_0(<n(x)>/n_0$ in the notation of the present paper-dashed curve), and the reflectivity R (in arbitrary units). the maximum of R was about 1.2%. The solid line with dots is the time averaged profile $<|E_1(x)|^2>$ of the SRS daughter LWs, , in units of the decay threshold $E_T$.b. Time averaged modal spectrum $<|E(k)|^2>/16\pi n_0T_e$ versus $k/k_D$ for this case. The inset is an enlargement of the peak near $k_1\lambda_D=0.125$.

Figure 14. From [39]: The local relationship between the modulus squared of the envelope of the daughter LWs, $<|E_1|^2>$, (in units of the decay threshold $E_T{}^2$ and the local source $S$, in units of the linear source threshold amplitude $S_T$). Top curve: $L/\lambda_0=45, I/I_T=26$. Next lowest curve -same as Fig. 13. Third curve: $L/\lambda_0=22.5, I/I_T=130$ and $\nu_{ei}$ is half that of Fig.13. Bottom curve: $L/\lambda_0=22.5, I/I_T=128$.Unless otherwise stated the parameters are the same as for Fig. 13. Boxes: Determined from homogeneous turbulence simulations.

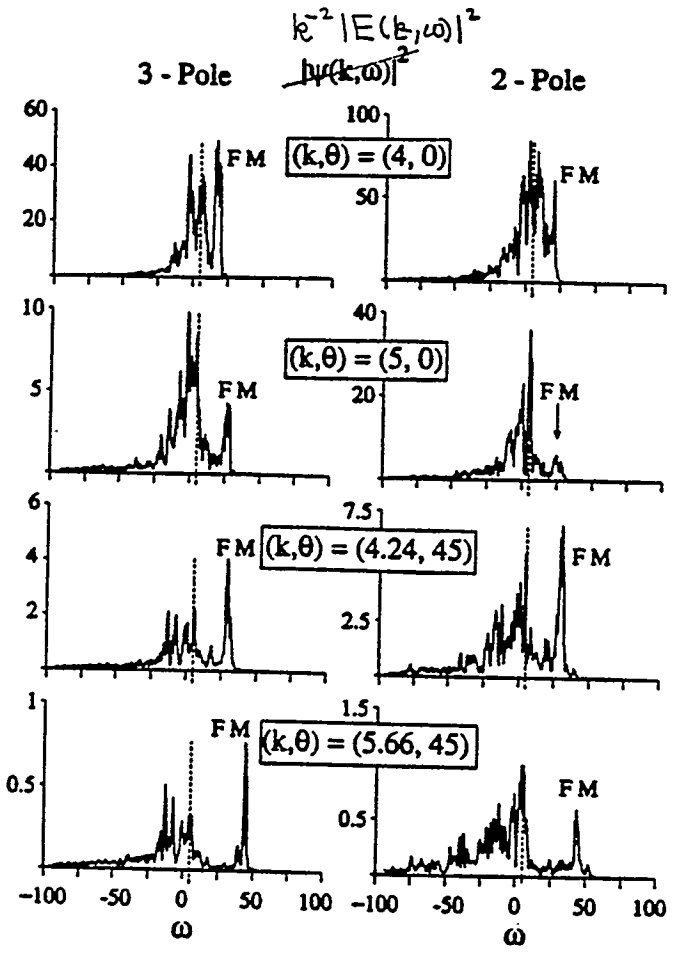
$k^{-2}|E(k,\omega)|^2$
3 - Pole
$|\psi(k,\omega)|^2$
2 - Pole
(k,θ) = (4, 0)
(k,θ) = (5, 0)
(k,θ) = (4.24, 45)
(k,θ) = (5.66, 45)
FM
ω

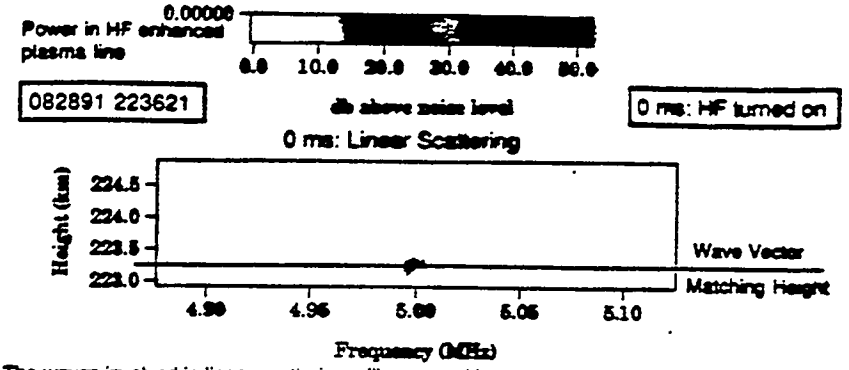


The waves involved in linear scattering will grow and become unstable resulting in parametric instabilities; this is weak turbulence theory.

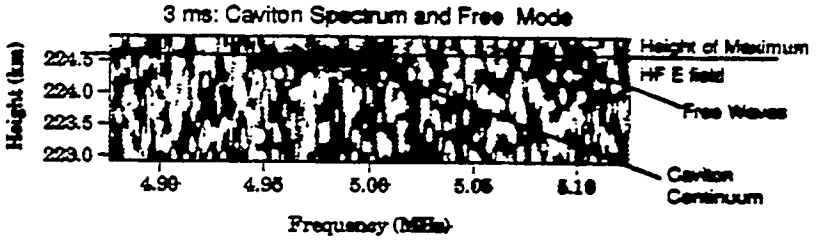


SLT effects come quickly: scatter from waves inside cavitons and free waves generated by the disturbance are seen very near the HF reflection Height where the HF E field is strong.

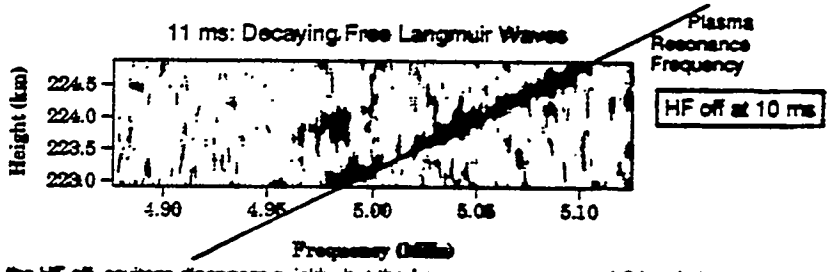


With the HF off, cavitons disappear quickly, but the free waves, seen over 1.8 km, fade slowly.

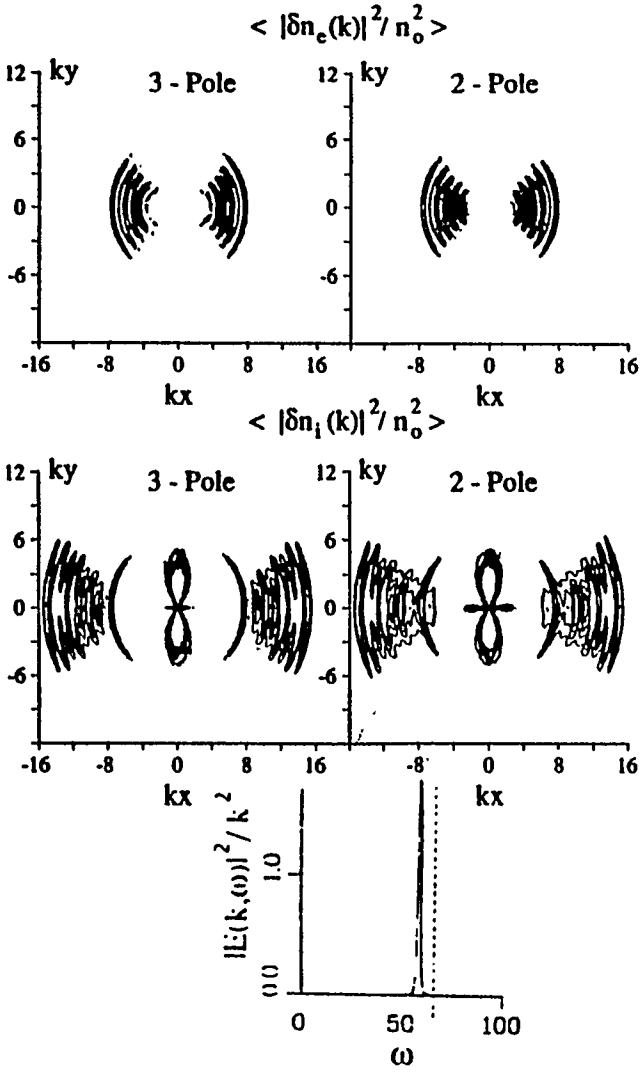
< |δn_e(k)|^2 / n_o^2 >
3 - Pole
2 - Pole
ky
kx
< |δn_i(k)|^2 / n_o^2 >
|E(k,ω)|^2 / k^2
ω

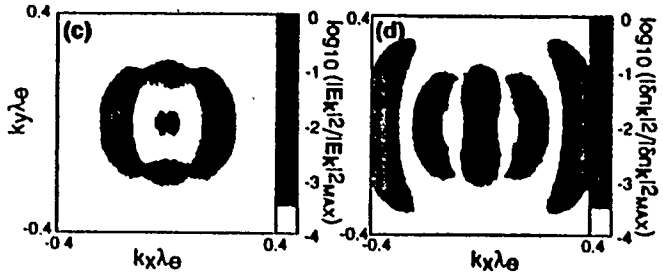
(c)
(d)
kyλe
kxλe
log10 (|Ek|2/|Ek|2max)
log10 (|δnk|2/|δnk|2max)

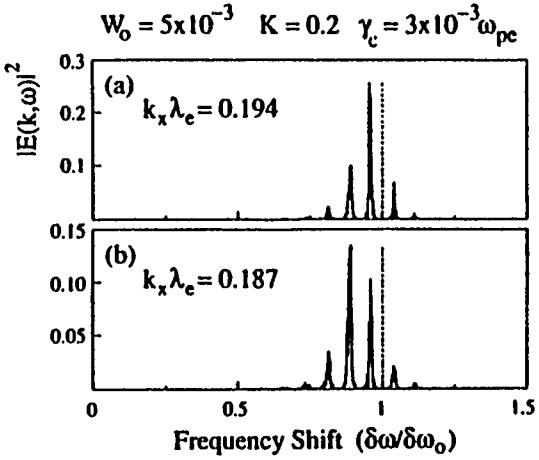
W_o = 5x10^-3 K = 0.2 γ_c = 3x10^-3 ω_pe
|E(k,ω)|^2
(a) k_xλ_e = 0.194
(b) k_xλ_e = 0.187
Frequency Shift (δω/δω_o)

$n_o/n_C = 0.244$

$E_o/E_T = 4$

$E_o/E_T = 8$

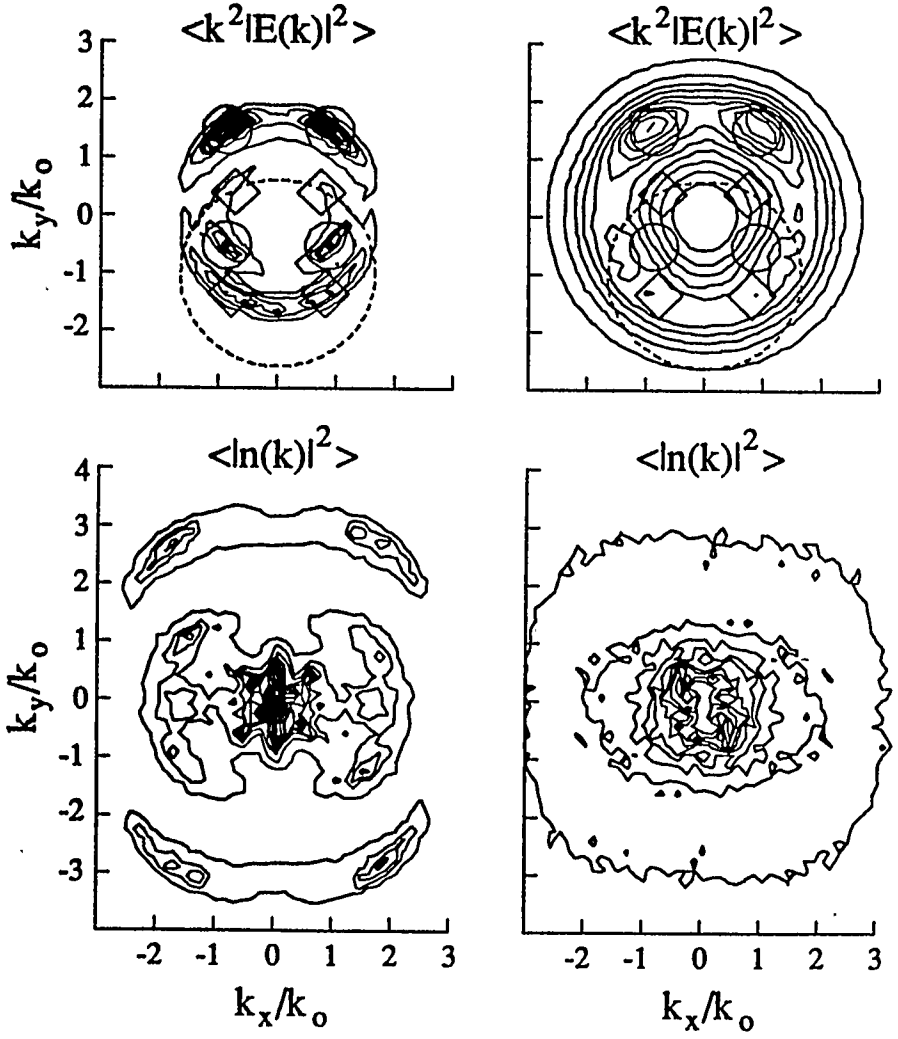


$n_o/n_C = 0.234$

$E_o/E_T = 4$

$E_o/E_T = 8$

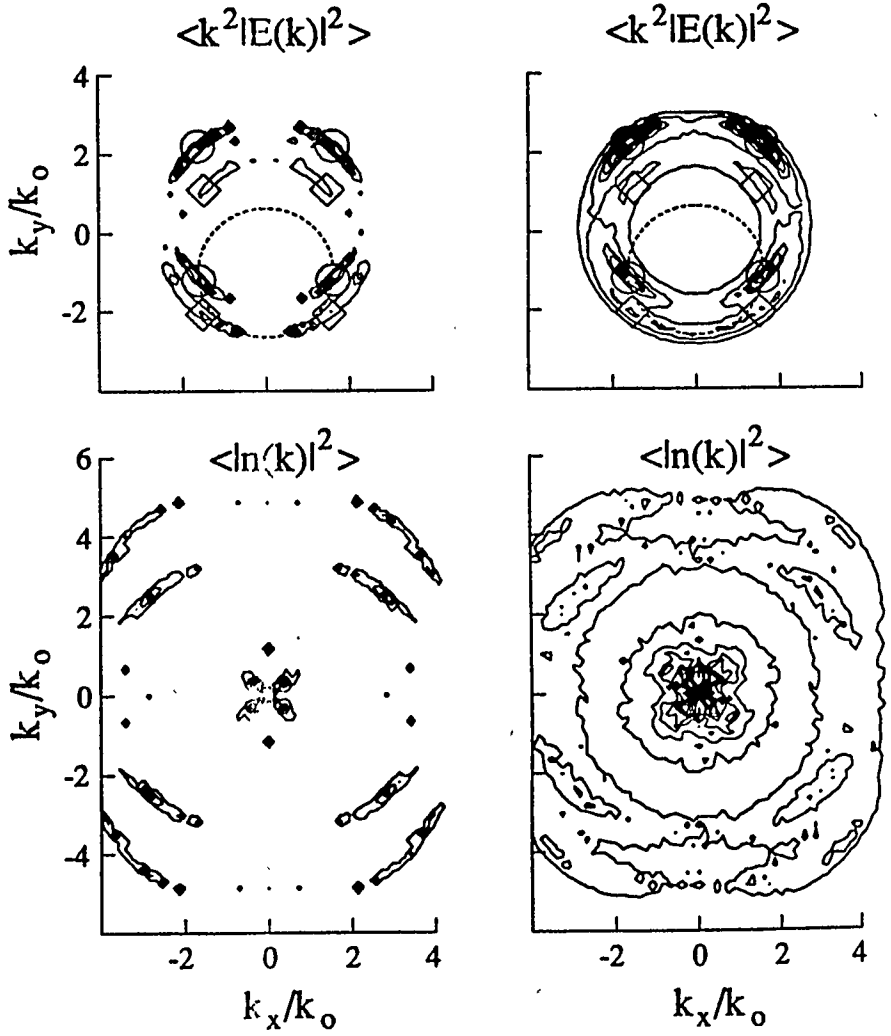

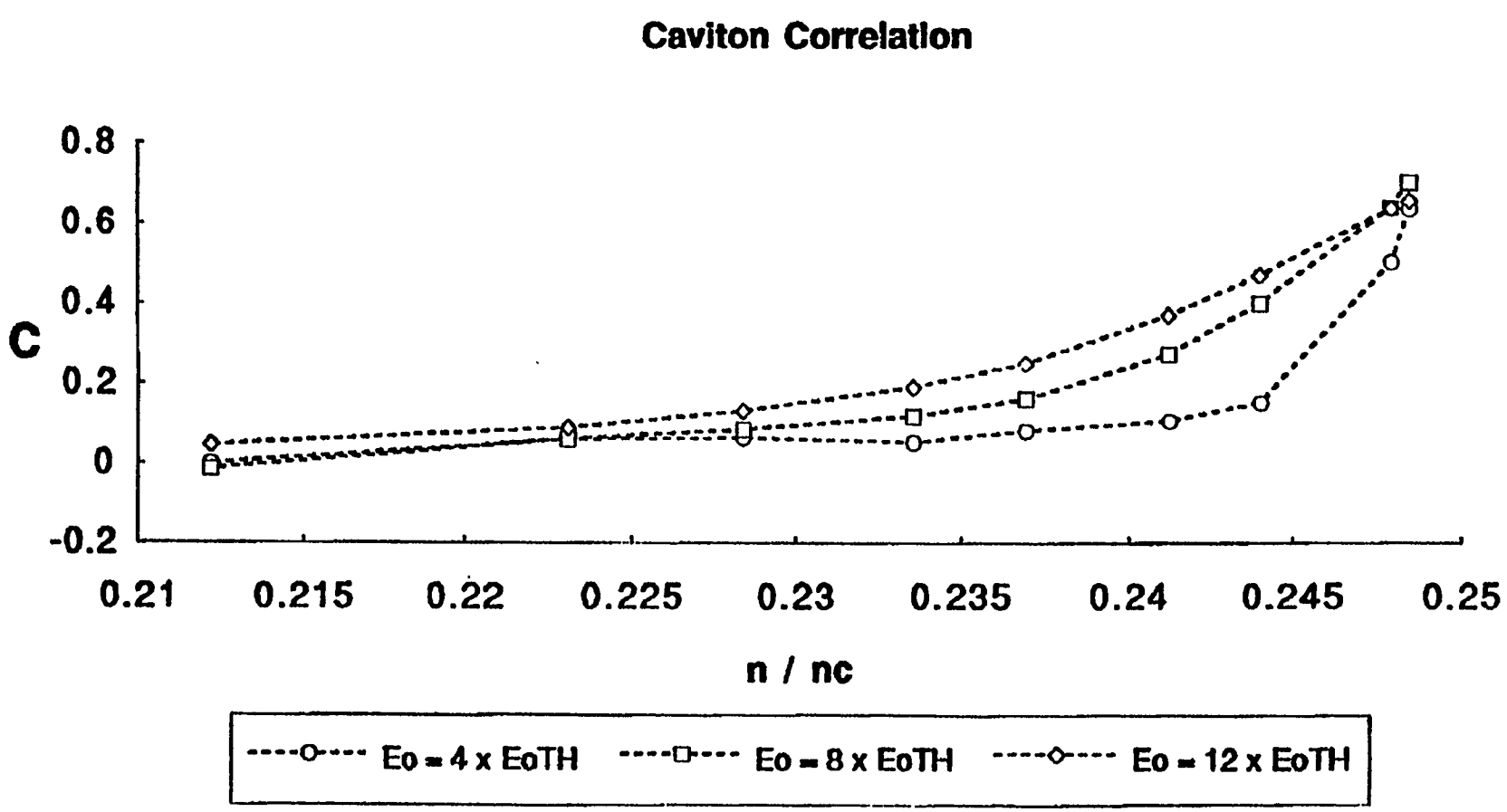
Caviton Correlation
0.8
0.6
0.4
0.2
0
-0.2
C
0.21
0.215
0.22
0.225
0.23
0.235
0.24
0.245
0.25
n / nc
Eo = 4 x EoTH
Eo = 8 x EoTH
Eo = 12 x EoTH

$$\langle |J_{3/2}(k_{3/2},\theta)|^2 \rangle$$

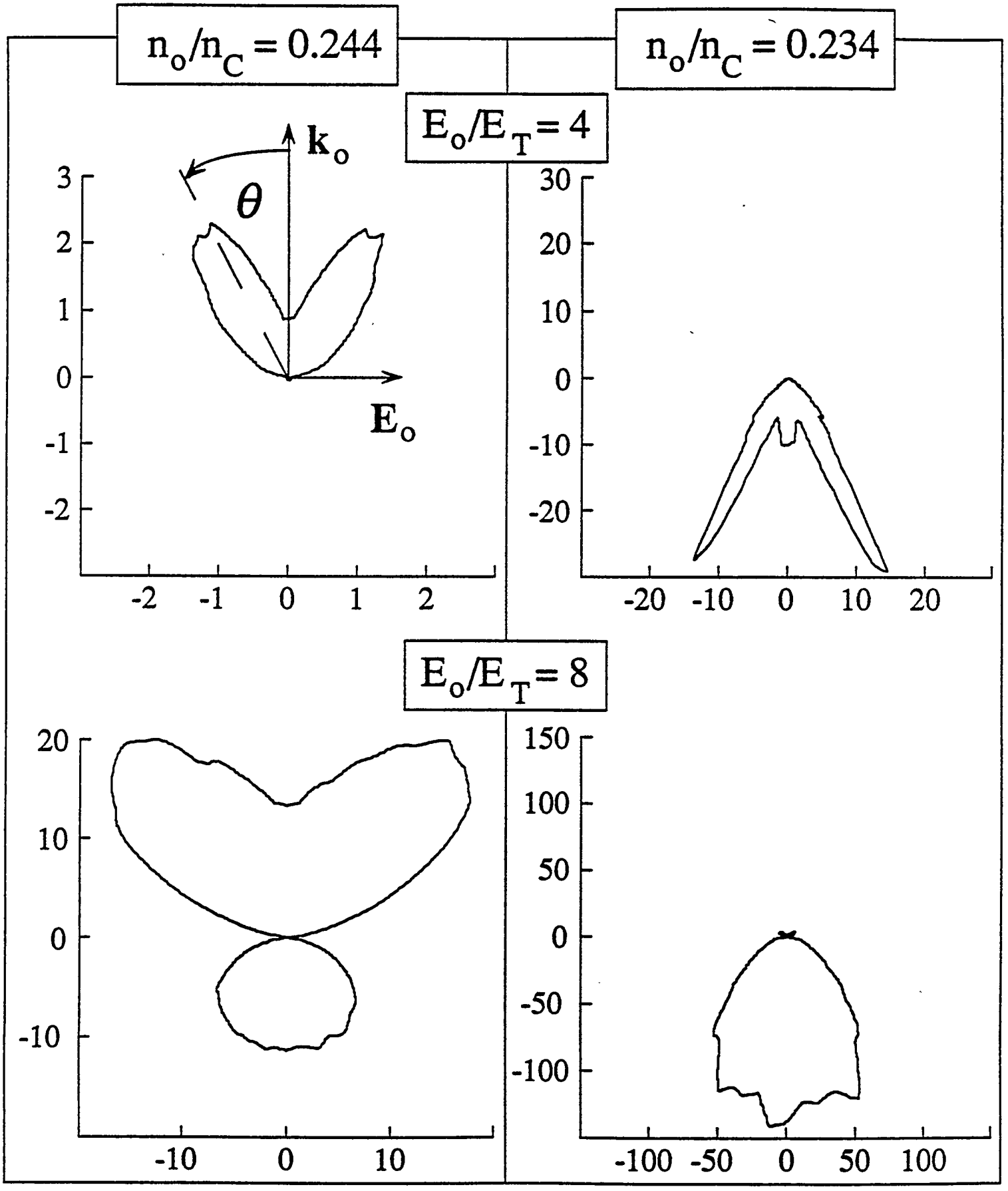

$$\langle |J_{3/2}(k_{3/2},\theta,\omega)|^2 \rangle$$

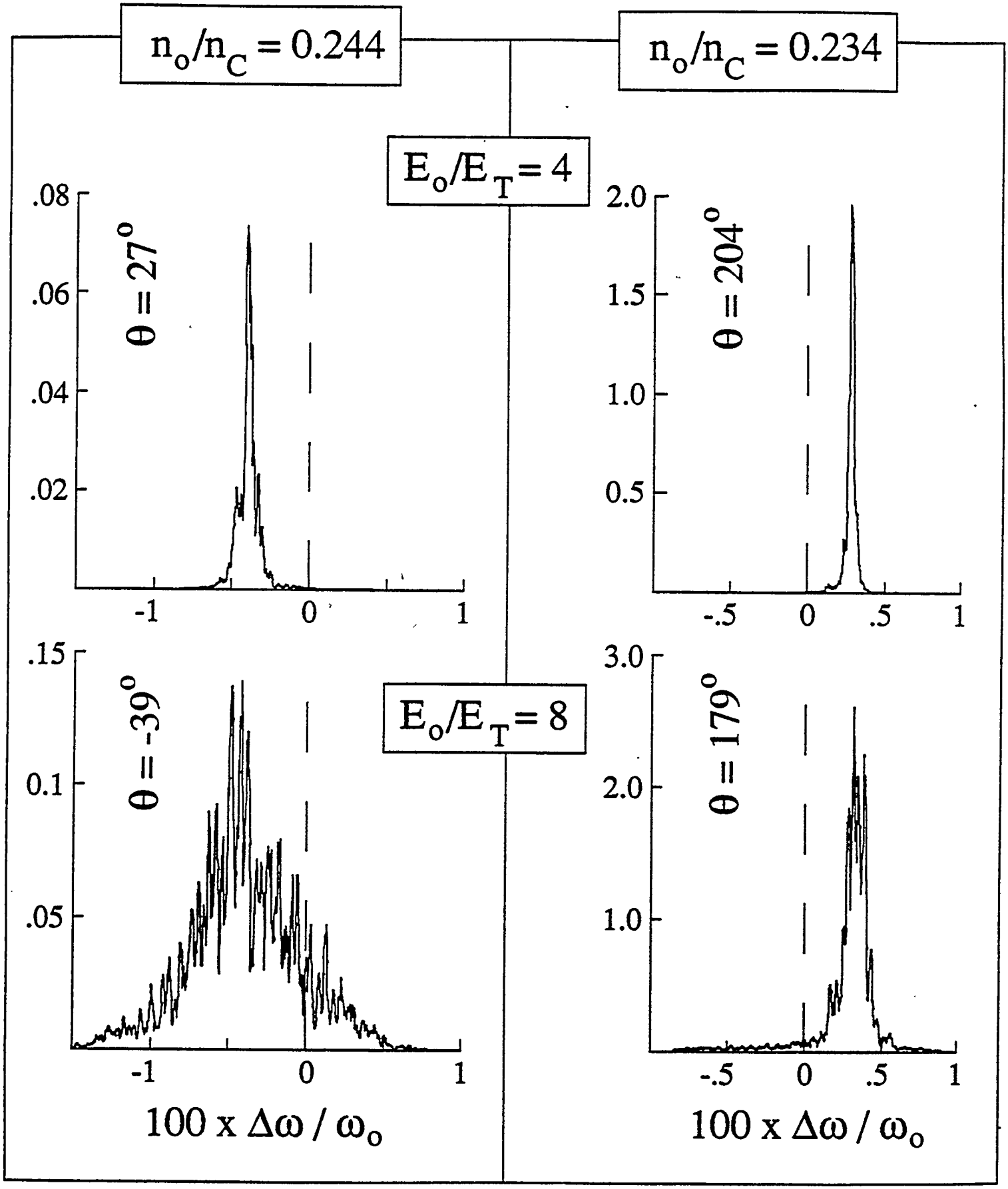

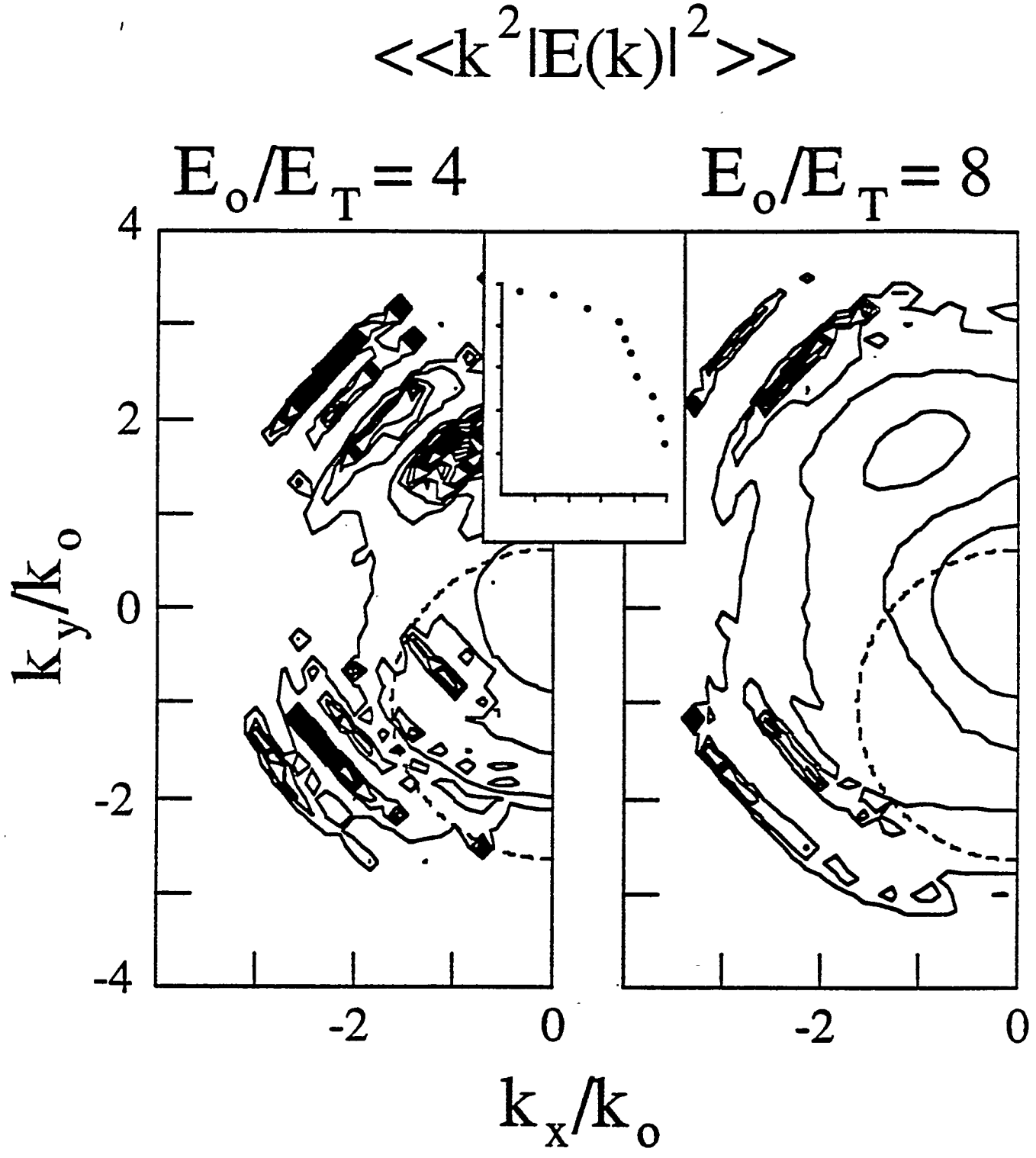
<<k²|E(k)|²>>
E₀/E_T = 4
E₀/E_T = 8
4
2
0
-2
-4
k_y/k_o
-2
0
-2
0
k_x/k_o

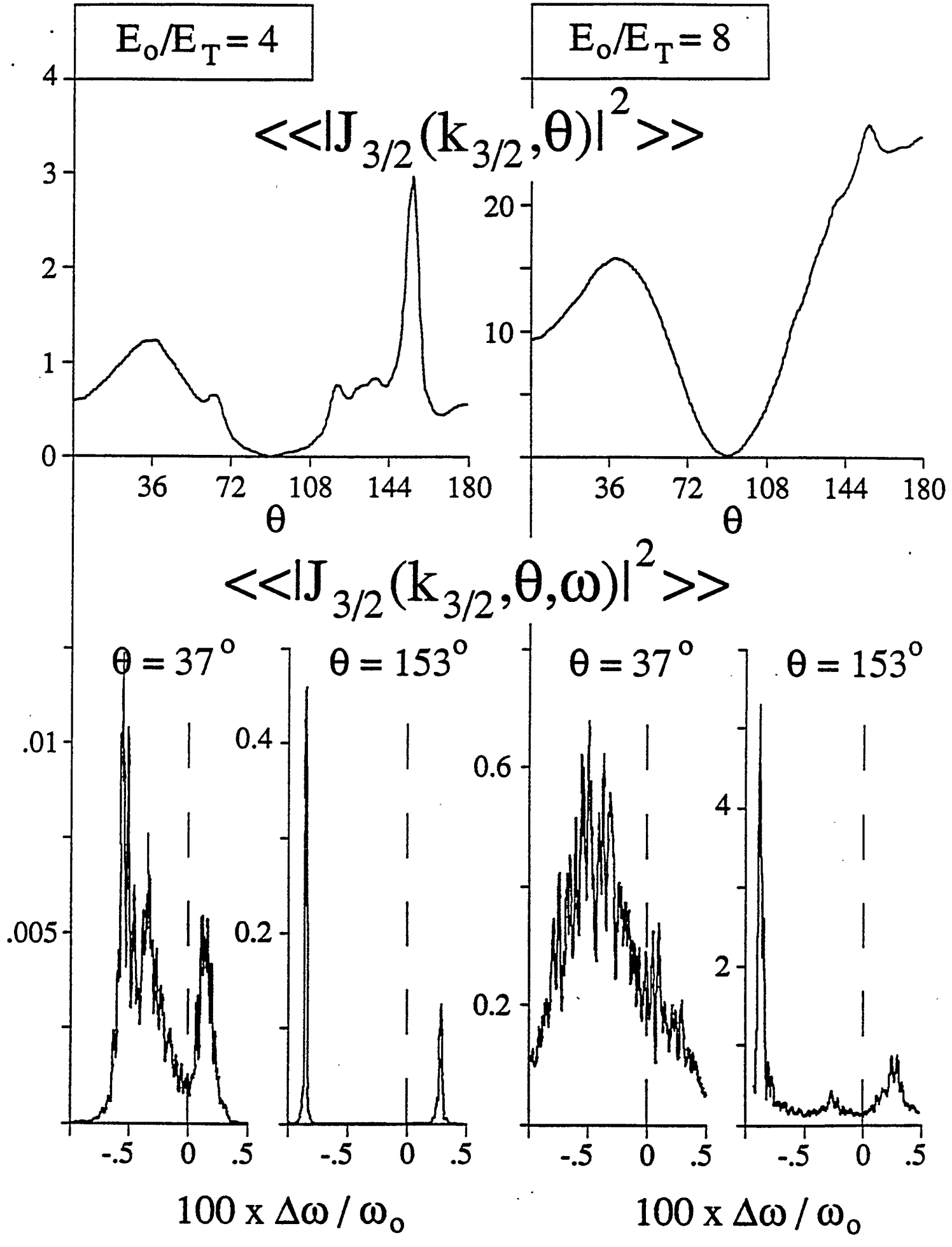
$E_o/E_T = 4$
$E_o/E_T = 8$
$\langle\langle |J_{3/2}(k_{3/2},\theta)|^2 \rangle\rangle$
4
3
2
1
0
20
10
36
72
108
144
180
θ
$\langle\langle |J_{3/2}(k_{3/2},\theta,\omega)|^2 \rangle\rangle$
θ = 37°
θ = 153°
θ = 37°
θ = 153°
.01
.005
0.4
0.2
0.6
0.2
4
2
-.5
0
.5
100 x Δω / ω_o
100 x Δω / ω_o

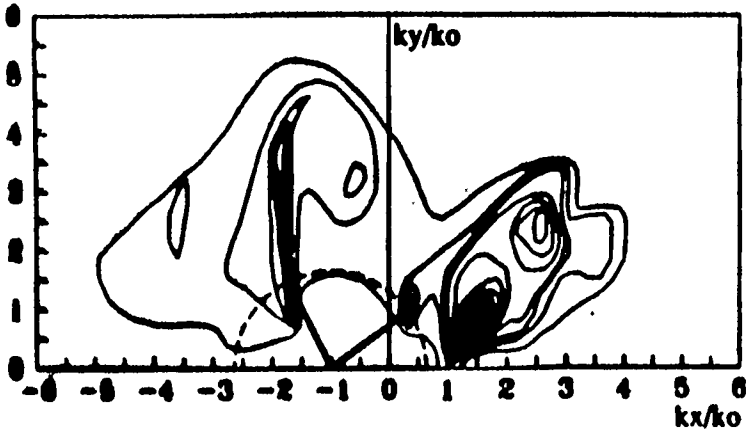


a

**FIG. 3. Contours of the saturated TPD wave intensity in space obtained from streak records**

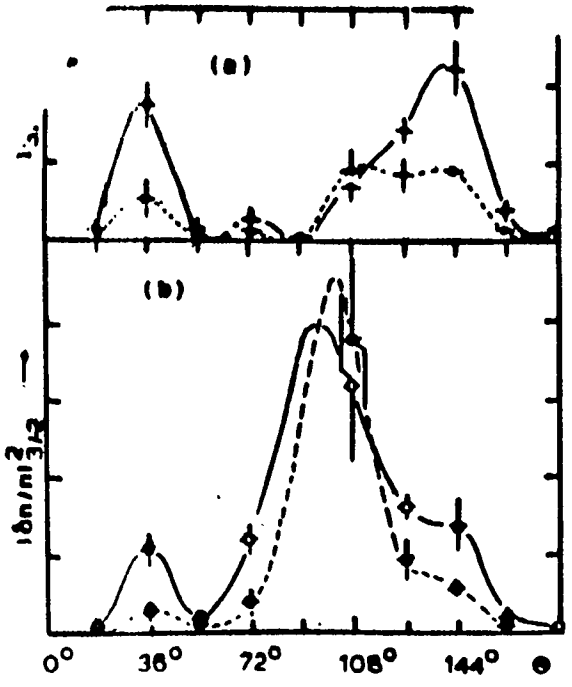


b

FIG. 2. The $(3/2)\omega_0$-intensity and plasmon intensity distributions. (a) Angular $(3/2)\omega_0$-intensity distribution for two laser energies (●: 4.5 J, ○: 6.5 J). Error bars indicate the accepted angular range and the standard deviation over several experiments. (b) Plasmon intensity distribution for

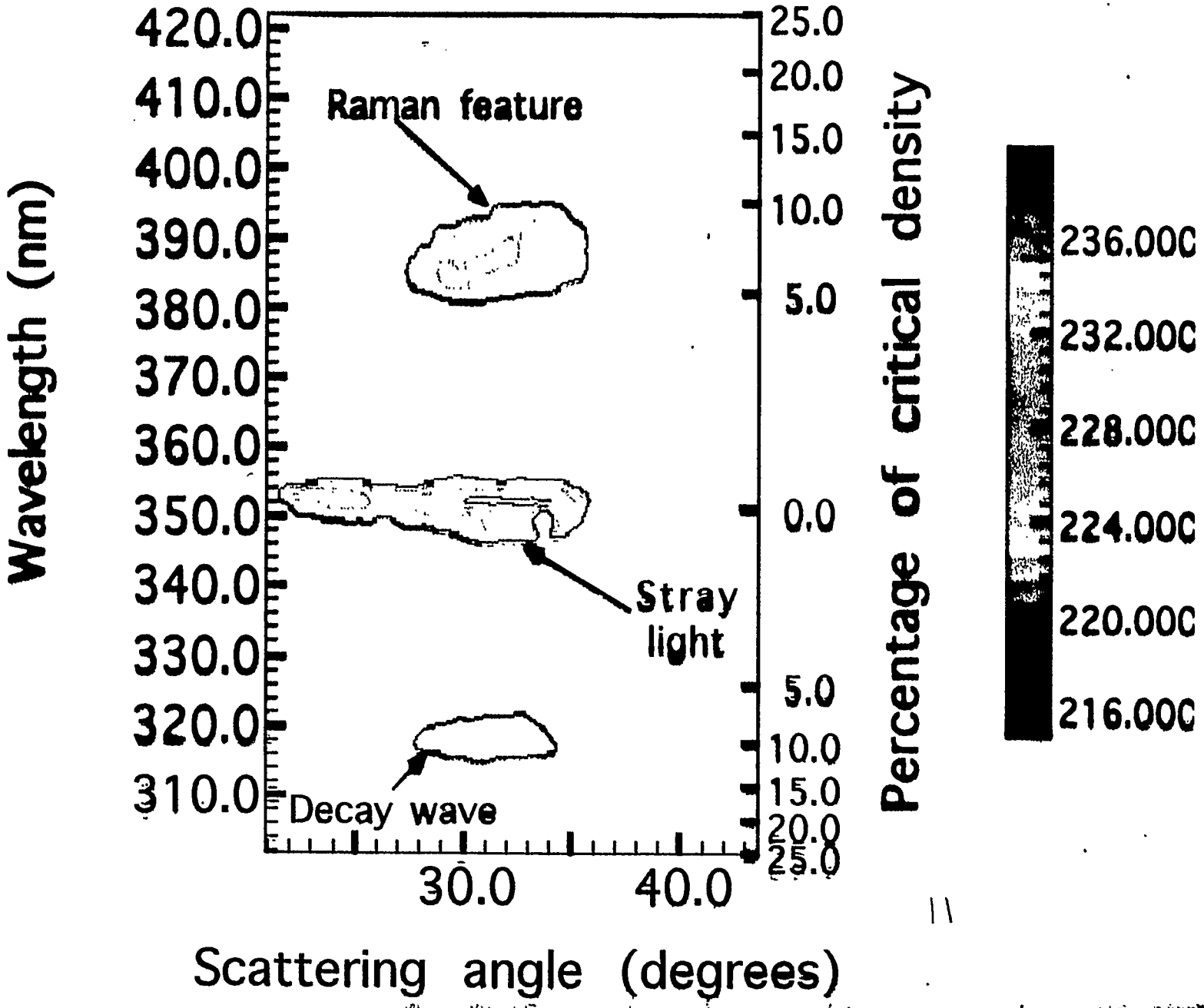
Wavelength (nm)
420.0
410.0
400.0
390.0
380.0
370.0
360.0
350.0
340.0
330.0
320.0
310.0
Raman feature
Stray light
Decay wave
25.0
20.0
15.0
10.0
5.0
0.0
5.0
10.0
15.0
20.0
25.0
30.0
40.0
Scattering angle (degrees)
Percentage of critical density
236.00C
232.00C
228.00C
224.00C
220.00C
216.00C

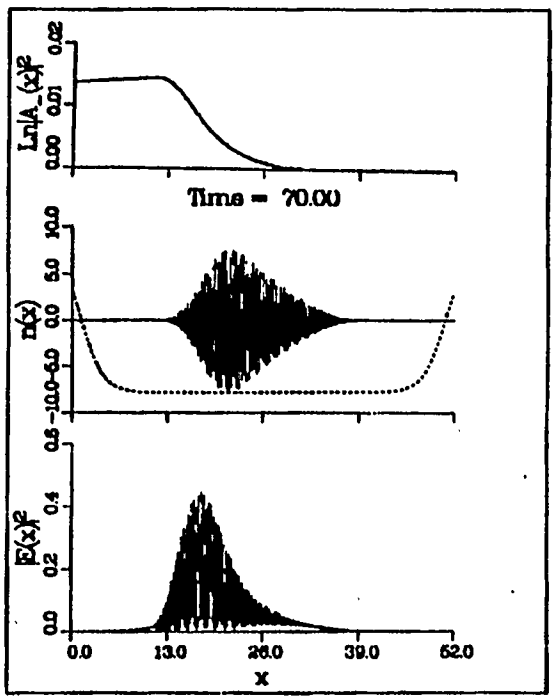
Ln|A_(x)|²
0.02
0.01
0.00
Time = 70.00
n(x)
10.0
5.0
0.0
-5.0
-10.0
|E(x)|²
0.6
0.4
0.2
0.0
0.0
13.0
26.0
39.0
52.0
x

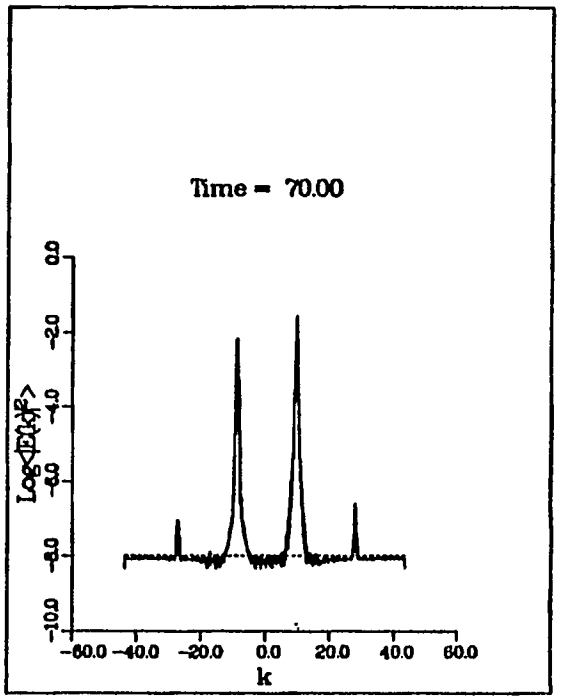
Time = 70.00
Log<|E(k)|²>
0.0
-2.0
-4.0
-6.0
-8.0
-10.0
-60.0
-40.0
-20.0
0.0
20.0
40.0
60.0
k

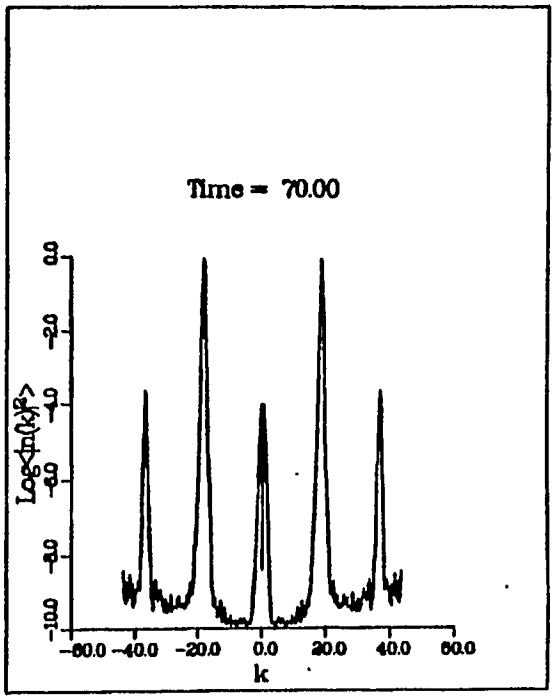
Time = 70.00
Log<|n(k)|²>
0.0
-2.0
-4.0
-6.0
-8.0
-10.0
-60.0
-40.0
-20.0
0.0
20.0
40.0
60.0
k

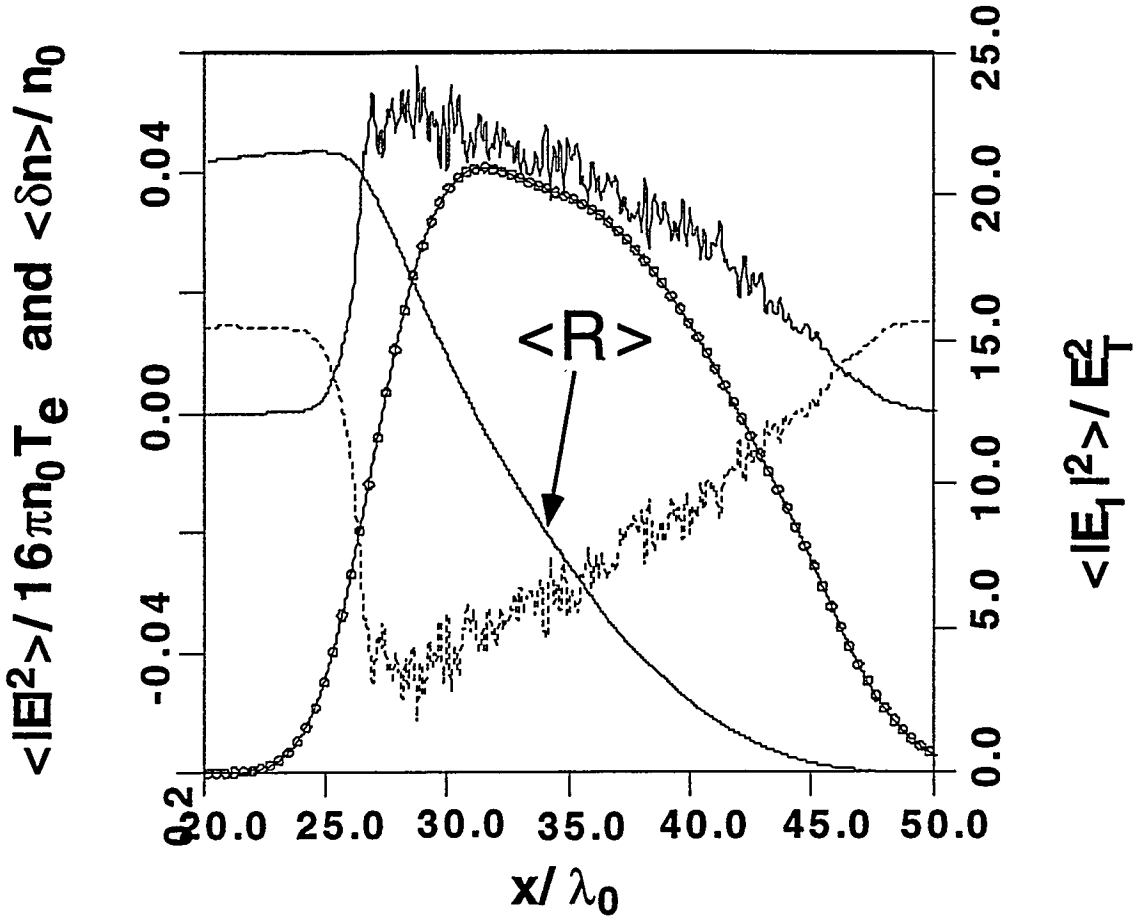
<E2>/16πn0Te and <δn>/n0
0.04
0.00
-0.04
-0.2
20.0 25.0 30.0 35.0 40.0 45.0 50.0
x/λ0
<R>
25.0
20.0
15.0
10.0
5.0
0.0
<|E1|2>/E2T

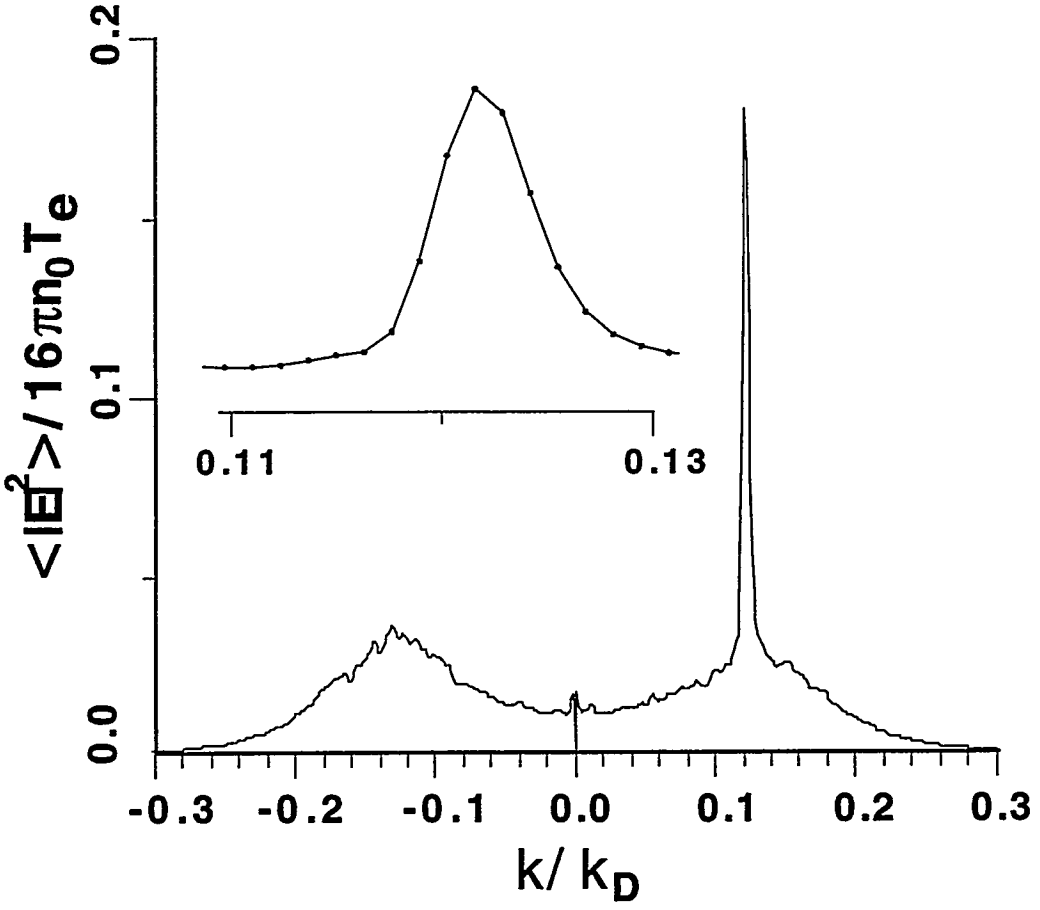
<E2>/16πn0Te
0.2
0.1
0.0
0.11
0.13
-0.3 -0.2 -0.1 0.0 0.1 0.2 0.3
k/kD

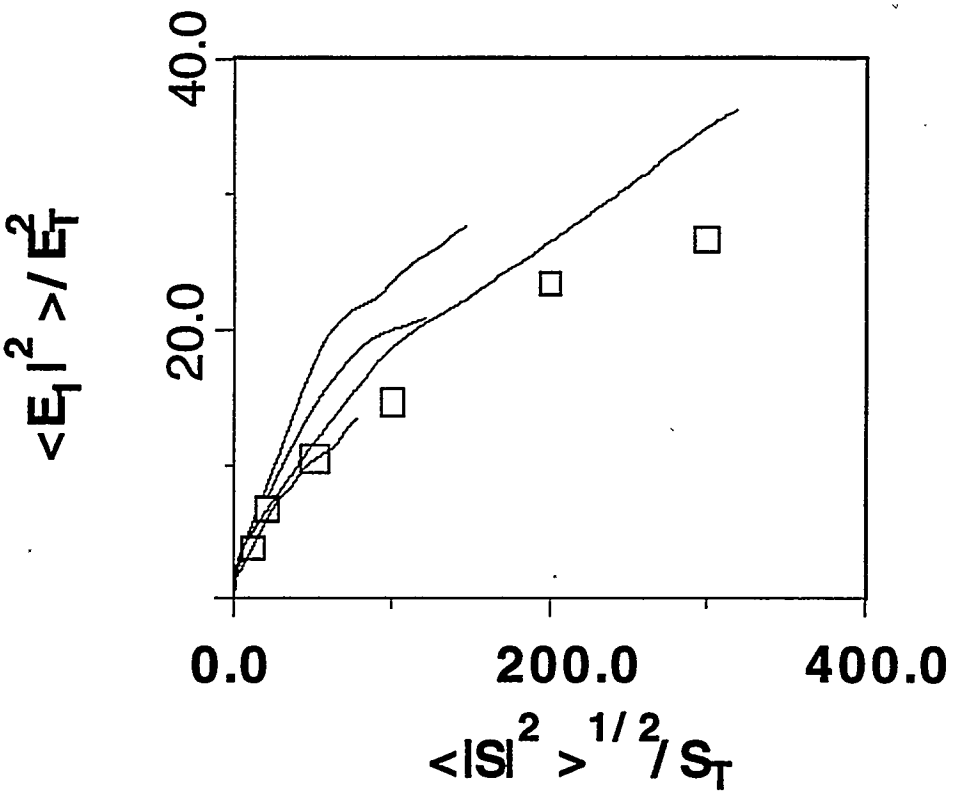


## DISCLAIMER